universität wien

MASTERARBEIT / MASTER'S THESIS

Titel der Masterarbeit / Title of the Master's Thesis

„Atmospheric Evolution of the Habitable Zone Sub-Neptune K2-18 b“

verfasst von / submitted by

Thorben Alexander Johannes Frey, BSc

angestrebter akademischer Grad / in partial fulfilment of the requirements for the degree of

Master of Science (MSc)

Wien, 2023 / Vienna, 2023

Studienkennzahl lt. Studienblatt / degree programme code as it appears on the student record sheet:	UA 066 861
Studienrichtung lt. Studienblatt / degree programme as it appears on the student record sheet:	Masterstudium Astronomie
Betreut von / Supervisor:	Ass.-Prof. Dr. Sudeshna Boro Saikia

Acknowledgements

First of all, I would like to thank Ass.-Prof. Dr. Sudeshna Boro Saikia, my thesis supervisor, who supported me throughout my research by providing input and answering my questions at every time, even though she had a lot on her plate. Without her, this project would not have been possible! I would also like to thank Gwenaël van Loovren, who helped me set up and use the Kompot code, and who was always available in the office and to whom I turned every time I messed up my installations. I would also like to thank Simon Schleich for providing the theoretical transit spectra, which will allow me to better explain what needs to be done in the future. Furthermore, I would like to thank the members of the groups of Ass.-Prof. Dr. Sudeshna Boro Saikia and Univ.-Prof. Dipl.-Phys. Dr. Manuel Güdel, who all gave valuable input to my thesis at one point or another and had lunch or a little chat with me from time to time. Thanks to them, I was able to enjoy every day at the institute.

Last but not least, I would like to thank my girlfriend Hanna Hirt, who not only helped me to improve the language and style of this thesis, but was also there for me as a mental support during this challenging and demanding time. There have been some rough patches on my way to this thesis and she has helped me through every single one of them. I could not have done it without her!

Abstract

K2-18 b is a sub-Neptune above the radius valley without a solar system analogue. The atmosphere was found to be dominated by H_2 and He with traces of H_2O and CH_4. The exact amounts of the trace gases as well as the atmospheric mass fraction and the nature of the exoplanets core are subject to recent studies.

As currently only snapshot models of the planet and its atmosphere exist, my master's thesis aims to investigate the short-term atmospheric evolution of K2-18 b by exploring different scenarios within the current constraints. Using the Kompot code developed at the University of Vienna, I performed multiple simulations considering over five hundred chemical reactions, including photochemical reactions. These simulations consider energy sources such as stellar radiation, atmospheric loss mechanisms, diffusion processes, as well as heating and cooling effects to provide a comprehensive analysis of the atmospheric evolution of K2-18 b.

My simulations show that the atmospheric lifetime hardly depends on the exact amount of water in the atmosphere, but on the fact whether water is existent or not. Furthermore, they disfavor the existence of a very lightweight atmosphere, as such an atmosphere should already have vanished taking stellar evolution and the lifetime of the system into account. Moderately massive atmospheres on the other hand might vanish within in the next 10 Gyr to 15 Gyr. This would enable the planet to outgas a primary or secondary atmosphere, which might be rich in heavier species. Additionally, my simulations show that a massive atmosphere would be stable long-term with a predicted lifetime around 4000 Gyr .

Kurzfassung

K2-18b ist ein Sub-Neptun oberhalb des *radius valley*, ohne ein Analogon im Sonnensystem. Es wurde festgestellt, dass die Atmosphäre von H_2 und He dominiert wird und Spuren von H_2O und CH_4 enthält. Die genauen Mengen der Spurengase, sowie der Massenanteil der Atmosphäre und die Beschaffenheit des Exoplanetenkerns sind Gegenstand aktueller Forschung.

Da derzeit nur Momentaufnahmen des Planeten und seiner Atmosphäre existieren, zielt meine Masterarbeit darauf ab, die kurzfristige atmosphärische Entwicklung von K2-18b zu simulieren, indem ich verschiedene Szenarien innerhalb der derzeitigen Beschränkungen erforsche. Mit Hilfe des Kompot-Codes, der an der Universität Wien entwickelt wurde, habe ich mehrere Simulationen durchgeführt, die über fünfhundert chemische Reaktionen, einschließlich photochemischer Reaktionen, berücksichtigen. Diese Simulationen berücksichtigten Energiequellen wie stellare Strahlung, atmosphärische Verlustmechanismen, Diffusionsprozesse und Heiz-/Kühleffekte, um eine umfassende Analyse der atmosphärischen Entwicklung von K2-18b zu ermöglichen.

Meine Simulationen zeigen, dass die atmosphärische Lebensdauer kaum von der genauen Menge an Wasser in der Atmosphäre abhängt, sondern davon, ob Wasser im Gemisch vorhanden ist oder nicht. Außerdem sprechen sie gegen die Existenz einer sehr leichten Atmosphäre, da eine solche Atmosphäre unter Berücksichtigung von Sternentwicklung und der Lebensdauer des Systems bereits verschwunden sein müsste. Mäßig massive Atmosphären hingegen könnten innerhalb der nächsten 10 bis 15 Gyr verschwinden. Dies würde es dem Planeten ermöglichen, eine primäre oder sekundäre Atmosphäre auszugasen, die reich an schwereren Verbindungen sein könnte. Darüber hinaus zeigen meine Simulationen, dass eine massereiche Atmosphäre mit einer voraussichtlichen Lebensdauer von etwa 4000 Gyr langfristig stabil wäre.

Contents

List of Tables

List of Figures

1 Introduction

Across the sea of space, the stars are other suns.
– Carl Sagan, 1980

Although this sentence was spoken by one of the pioneers of exoplanetary science 15 years before the discovery of the first exoplanet, 51 Peg b (Mayor and Queloz 1995), it is more evident today than ever before. As the number of discoveries of exoplanets continues to grow and now has reached 5,438[1] exoplanets, we now assume that there are indeed more planets than stars in our Milky Way (Barclay et al. 2021). While the search for more exoplanets continues unhindered, questions about the appearance of those discovered already are being raised as well. One of the most intriguing questions being that of the habitability of these planets. Today we consider three factors to be the most important for habitability: the existence of a liquid, an atmosphere, and an abundance of nutrients. The latter is difficult to determine without in-situ measurements. Therefore, research focuses primarily on factors which can be measured from at least 4 light years away[2].

The earliest approach to classifying the potential habitability of planets was published two years before the discovery of 51 Peg b by Kasting, Whitmire and Reynolds 1993. Since water is known to be a liquid with the potential to support life, the habitable zone of a planet was defined as a distance from the host star which allows for the temperature on the exoplanet to remain between the melting and the boiling point of water. This definition is sometimes referred to as the *classical habitable zone*, as there are now more sophisticated models that consider different planetary parameters and therefore extend the habitable zone (Kopparapu et al. 2013). Examples of such planetary factors are the albedo of the planet's surface or the presence of an atmosphere. The atmosphere not only keeps the planet at a moderate temperature, but also keeps the surface pressurised, which prevents liquids from evaporating into space. Another significant role of the atmosphere, which is particularly relevant for this thesis, is the absorption of high-energy radiation. The best-known example on Earth is ultraviolet radiation, which is partially absorbed by the atmosphere, and is harmful to many known lifeforms. Remembering basic physical concepts, we know that energy cannot simply disappear. All absorbed radiation is converted into heat, raising the temperature of the upper atmosphere where it is absorbed. In Figure 1.1 a depiction of the Earth's atmsopheric structure is shown. Upper atmosphere in this case means the thermosphere and above.

Observing traces of an exoplanet's atmosphere is a relatively new possibility in the field of exoplanet research. The most common and productive method of measuring

[1] https://exoplanetarchive.ipac.caltech.edu/ on the 7$^{\mathrm{th}}$ of June 2023
[2] 4 ly is the distance to the nearest exoplanet, Proxima Centauri b, Anglada-Escudé et al. 2016

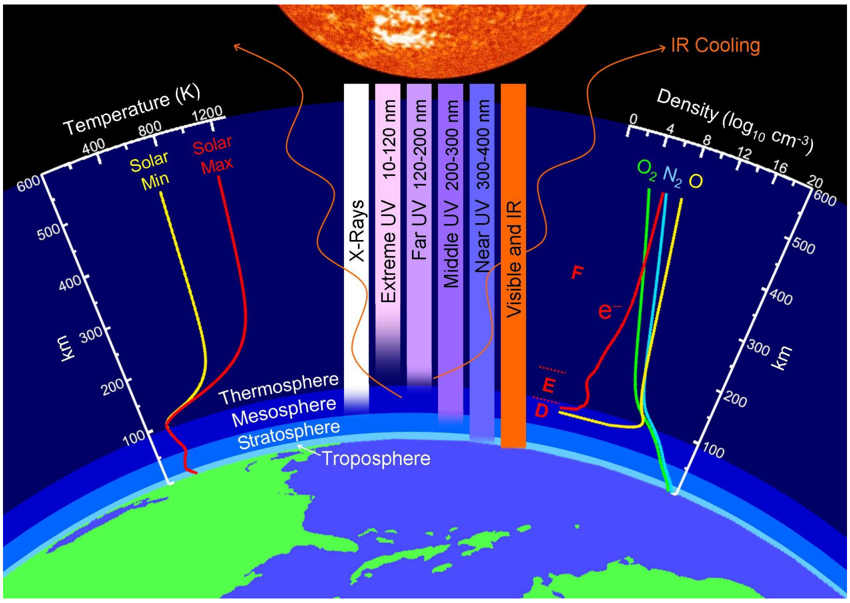

Figure 1.1: Depiction of the Earth's atmosphere with different layers. The upper atmosphere as I use the term includes the thermosphere and everything above for the Earth[3].

exoplanetary atmospheres is transit spectroscopy, where the transit of an exoplanet in front of its host star is observed not only with a photometer but also with a spectrograph. Initially, it was only possible to study the atmospheres of gas giants, mostly hot Jupiters, because of the greater influence on stellar spectra. But with modern instruments, e.g., HST (Dressel and Marinelli 2023), JWST (Rigby et al. 2022), prospect. Ariel, i.e. the future ESA space telescope especially designed for atmospheric studies of exoplanets, (Tinetti et al. 2020), it is also possible to look at smaller planets (Barclay et al. 2021). This is a crucial step, as gas giants are not habitable in any orbital configuration based on our current understanding of life.

In addition to this general assumption of habitability based on the type of planet, we can also narrow down which stars are suitable hosts. We know for sure that the Sun, and therefore G stars, can host a habitable planet. But life as we see it today took time to evolve, as does the planet. Evolution in its nature is not a fast process, life forms need a reasonably stable environment to develop, and not all stars live long enough and evolve slowly enough to provide this stable environment. It is thought that only F, G, K and M stars can host a habitable planet (Benneke et al. 2019). This stellar-influenced stability criterion applies not only to temperature, but also to the protective atmosphere mentioned above. If the atmosphere vanishes, any surface liquid will evaporate, reducing the prospects for habitability. In this thesis I will study an exoplanet that (prospectively) fulfils all the aforementioned requirements, but which's stability and evolution, as well as the exact nature of its atmosphere, remain unknown. The planet this thesis will focus on is K2-18 b, which orbits an M dwarf within its classical habitable zone of 0.159 AU. Its size and mass are between Neptune and Earth, and it has an atmosphere containing at least hydrogen and helium, accompanied by water or methane or both, and some other trace gases. Its equilibrium temperature is between 250K and 270K (Benneke et al. 2019, Cloutier et al. 2019), which is similar to Earth.

Although K2-18 b is one of the best-studied exoplanets, the actual data from observations is quite sparse. This leads to a large number of uncertainties, particularly in our knowledge of the atmospheric composition and the core-to-atmosphere mass ratio. Different scenarios include massive iron cores and Earth-like cores, and volume mixing ratios for H_2O and CH_4 between nearly 0 % and 15 % for water, and 7 % for methane.

In this thesis I will use the upper atmospheric code Kompot to simulate different scenarios of the atmosphere of K2-18 b investigating its chemical and thermel profile, and hence, sharpen the picture of the potential habitability of this exoplanet. In order to narrow down the proposed scenarios, the short-term evolution of the planet's atmospheric composition and mass will be simulated. The simulations include constraints from observational and theoretical studies of planet formation and atmospheres.

2 Theoretical Background

Before going into detail about K2-18 b and its host star, this chapter describes the key terminology related to planetary science and atmospheric escape and evolution. In order to make this topic more tangible, I will use our Solar System as an example in many cases. But it will quickly become clear that this approach reaches its limitations with exoplanets and especially exoplanets like K2-18 b as the Solar System cannot depict the wide variety of exoplanets. In order to still be able to talk about our findings in a feasible way, astronomers came up with additional terminologies, which this chapter will explain.

2.1 Planetary Classification

Our Solar System has eight planets of different sizes, masses, and natures. From Jupiter, the largest and most massive, to Mercury, the smallest and lightest. If you study them, you soon realise that although each planet is special in its own way, some are more similar than others.

A rough classification which can be applied divides planets into two groups, gaseous and rocky – sometimes also terrestrial – planets. This classification divides our Solar System into two equal parts, four rocky and four gaseous planets (Lissauer and Pater 2013). The rocky planets, Mercury, Mars, Venus, and Earth are often divided into two further sub-classifications. Venus and Earth are Earth-like planets, Mars and Mercury are considered Mars-like or sub-Earths due to their smaller radius and mass. *Rocky* in this case does not necessarily indicate the absence of a gaseous envelope or atmosphere, it simply illustrates the fact that most of the mass is contributed to the core of the planet (Wordsworth and Kreidberg 2022). The same can be said of the more massive, gaseous planets. Jupiter and Saturn, the two largest and most massive planets in our Solar System, are often grouped together as gas giants or Jupiters. The two smaller giants are usually called ice giants or Neptunes (Lissauer and Pater 2013).

This classification works well for our Solar System, but quickly reaches its limits when it comes to exoplanets. Today there are 5,312 confirmed exoplanets listed in the NASA Exoplanet Archive 2023 [1] nearly 2,000 are between the magnitudes of Earth and Neptune ($1.4\ R_\oplus < R_{\text{Planet}} \leqslant 3.0\ R_\oplus$), as shown in Figure 2.1. So, nearly half of found exoplanets have no Solar System analogue and therefore, do not fit in the classification of Jupiters, Neptunes, Earth-like planets, and mini-Earths. Astronomers came up with several names for this ambiguous group of planets, *transitional exoplanets* being the least restrictive one, other names are *sub-Neptunes*, *super-Earths* or *mini-Neptunes*. All these terms, intentionally or not, put additional biases on the planet found, even though there may not

[1] Accessed on 30.03.2023 at 09:18, returning 34,084 lines.

be enough information to constrain the nature of the planet. If we speak of sub-Neptunes, we expect a gaseous planet, and conversely a rocky planet if the term super-Earth is used. It is therefore necessary to draw a clear demarcation line in this nebulous regime of extrasolar planets. In order to make this clean cut between super-Earths and sub-Neptunes, the density of the planets is the critical parameter. According to the definition of Wordsworth and Kreidberg 2022 a planet is rocky if its density is between that of pure silicate ($MgSiO_3$) $\rho_{\mathrm{min}} = 3.19\ g\ cm^{-3}$ [2] and pure iron (Fe) $\rho_{\mathrm{max}} = 7.87\ g\ cm^{-3}$ [2]. These elements were chosen because they make up the dense core of the Earth as well as its looser crust. Any planet less dense than silicate is classified as gaseous. Hereinafter, this study will consider rocky transitional exoplanets as super-Earths and gaseous transitional exoplanets as sub-Neptunes.

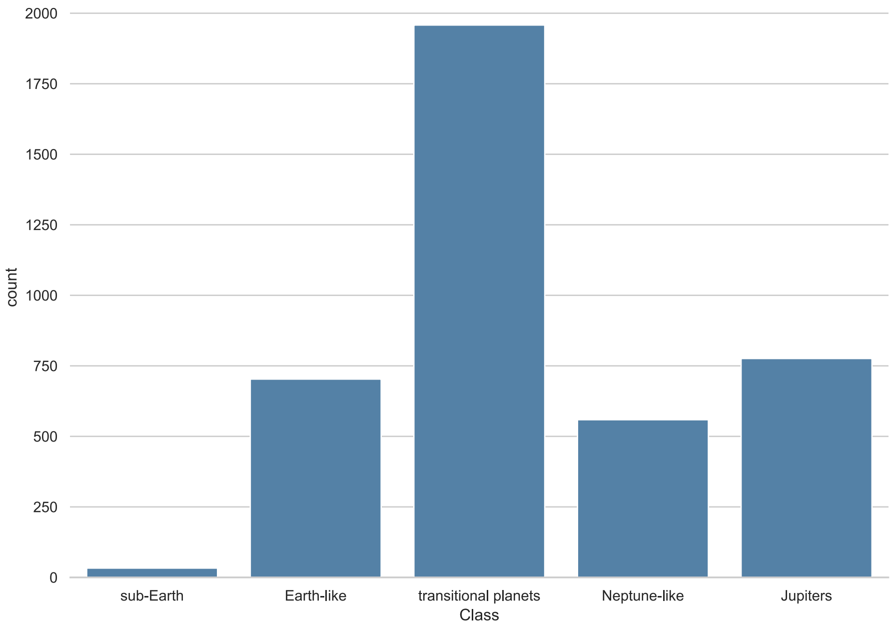

Figure 2.1: Statistic of discovered exoplanets based on the data set obtained from the NASA Exoplanet Archive 2023[1]. It is clearly visible that transitional exoplanets with a radius between Earth and Neptune are the most common.

[2] *CRC handbook of chemistry and physics : a ready-reference book of chemical and physical data* 1977

2.2 Planetary Atmospheres: Formation, Evolution and Loss

If we want to understand which kind of atmosphere we observe for any planet and make predictions on atmospheric composition, it is first necessary to understand how atmospheres form. Due to different formation scenarios the appearance of an atmosphere can differ a lot. It begins with the formation of the planet and the nature of the protoplanetary disk (Meadows 2008). In addition, the size of the planet, the type of host star, and many other factors, such as the dynamical stability of the system, have a strong influence on the atmosphere that can be observed.

2.2.1 Pathways of Atmospheric Formation

The ways in which planets can accrete atmospheres are manifold and are influenced by the circumstances of the planet's formation, the nature of the planet's core, and the radiation from the host star. In the following the formation history of planets will be considered, but other effects, such as orbital dynamics, *Grand Tack* [3], etc. will be left out of this thesis, as they are not relevant to the discussion as they do not have a major influence on the atmospheric composition.

Primordial Atmospheres

To understand the accretion of atmospheres properly, it is important to start with the proto planetary disc just after the formation of the host star. For the chemical composition of this atmosphere an elementary but important assumption is that the proto planetary disc has the same chemical composition as the star itself (Catling 2017). But the configuration of an atmosphere first requires a planet to form. As far as we know from observing the Solar System, the pathways of planet formation and atmosphere accretion are similar for rocky and gaseous planets. It is widely assumed that planet formation begins with small perturbations in the proto planetary disc. These perturbations occur simultaneously at several positions and coagulate small particles (µm size) of dust and gas. Through various processes, these microparticles grow from larger dust particles to pebbles, from small rocks to boulders, and from planetary embryos to protoplanets (Catling 2017, Armitage 2020). As some objects will always grow faster than others, these larger and more massive objects have a major influence on the evolution of the smaller objects. It is assumed that once the protoplanet mass, or later the core mass, exceeds 10-15 $M_\oplus$, the core begins to rapidly collect gas and dust from its sphere of influence, and thus may be taking in material that would otherwise have been collected by another smaller object at some point. Other factors that can support this so-called oligarchic growth for these planetary forebearers are relatively close orbits and the location of the snow line in the stellar system. A closer orbit results in a shorter orbital period, allowing the protoplanet to sweep its orbit more thoroughly in a shorter period. Beyond the snow line, the water contained in the proto planetary disc freezes into small ice particles, providing an additional source of solid matter that allows the protocore to grow even faster (Catling 2017). An example

[3] See Armitage 2020 for further reading

which combines these two mechanisms in very efficient manner is Jupiter. In our Solar System, the snow line is at ~ 5 AU, so the ideal point to form a massive planet would be just behind it to maximise the influence of the two effects mentioned. This is where Jupiter orbits.

Protoplanets smaller than 10 $M_\oplus$, on the other hand, collect gas much less efficiently than the larger ones. They also start later because they need more time to grow to a mass where they can bind gas and build a shell. Therefore, these envelopes are much smaller and contribute less to the total mass of the future planets.

In this thesis, the term *primordial atmosphere* is used to refer to this type of early envelope, which, like the solar nebula in the proto planetary disc, contains mainly molecular hydrogen and atomic helium (Johnstone 2017). The exact total mass of the heavier species that can be built up by accretion from the proto planetary disc is unclear and depends on the composition of the proto planetary disc, but some rough estimates can be made. To begin with, it is necessary to know or at least estimate the mass of the proto planetary disc, Gaidos 2017 predict a minimum mass of $M_{\text{PPD}} \simeq 9 \cdot 10^{-3} M_\odot$ for M dwarfs as observed by *Kepler*. Mercer and Stamatellos 2020 on the other hand predict a mass of at least $0.3 - 0.6\ M_*$ to drive planet formation due to disk instability. The resulting values for M dwarfs would be an order of magnitude higher than the one predicted by Gaidos 2017. However, these values are unlikely to apply to this thesis, as Mercer and Stamatellos 2020 put constraints on their simulation that do not fit the data presented in chapter 3.

In a study by Molyarova et al. 2017 several species as mass tracers for the mass of proto planetary disc, including H_2O, were investigated. They determined the mass of the different species in the proto planetary disc as a function of its total mass. They were able to place constraints on many of them, such as CO, CO_2, and H_2O (see Figure 1 and 2 in Molyarova et al. 2017). A rough estimate for masses between $10^{-4} M_\odot < M_{\text{PPD}} < 10^{-1} M_\odot$ would be that 0.01% of the total mass of the proto planetary disc is water. Therefore, if a planetary atmosphere is found to exceed this ratio of water (or any other element) to the proto planetary disc, it should be considered that the planet is no longer surrounded by its primordial atmosphere.

While this metal-poor primordial atmosphere is also called primary atmosphere in some older publications, I will use this term to describe the abundance of trace gases and the occurrence of certain effects that can shape the nature of the atmosphere (Catling 2017, Armitage 2020).

Primary and *Secondary Atmospheres*

Primary and *Secondary* atmospheres are more complex and varied than primordial ones, containing more species and being formed by planetary processes and stellar irradiation. Although it is possible that the atmosphere is still dominated by hydrogen and helium the amount of trace gases might be too high to be considered primordial. In most cases a significant amount of the originally bound envelope is lost to space through multiple escape processes (see subsection 2.2.2).

Immediately after formation – or after major impacts – the crust of the newly formed planet is hot enough for the surface to be covered by a magma ocean. The exact structure depends on the initial composition of the dust from which it was formed. How long the magma ocean can last depends on the physical properties of the material and on the existence of a primordial atmosphere, because even at low pressure ($\sim$ 0.1 bar) H_2 can act as a potent greenhouse gas and thus prolong their lifetime considerably (Wordsworth and Kreidberg 2022, Catling 2017). It is important to note that unlike water oceans, magma oceans freeze from the bottom up rather than from the top down. Therefore, the upper layer remains liquid for a long time and exchanges volatiles with the atmosphere. This can enrich the atmosphere with many different species containing oxygen, nitrogen, and carbon that were previously bound in the rocks that make up the magma ocean (Wordsworth and Kreidberg 2022, Johnstone 2017). Oxygen in particular is highly reactive and will interact with the other gases. Depending on the temperature and density of the atmosphere, different processes are dominant. Atmospheres formed by interaction with a magma ocean are referred to as *primary atmospheres.*

The *secondary atmosphere* results from a similar and more familiar process: volcanism. Volcanism occurs when the crust has solidified but the mantle and core are still liquid. As on Earth, there will always be parts of the crust that are weaker, and cracks and holes will appear. At these weak points, magma from below can push through the crust and reach the surface. Once at the surface, it behaves very much like a magma ocean, emitting volatiles which may contain a variety of species, such as CH_4, or react with the surface environment, like seawater, to form volatiles such as H_2O or CO_2 (Wordsworth and Kreidberg 2022, Johnstone 2017).

2.2.2 Escape Processes

A brief description of atmospheric escape process: A molecule or atom in the atmosphere remains bound if its kinetic energy is less than its gravitational potential energy. The gravitational potential is caused by the mass of the planet and the kinetic energy is related to the temperature of the atmosphere. The virial theorem connects these forms of energy from which we can draw the Jeans parameter (Wordsworth and Kreidberg 2022).

$$\lambda = \frac{E_{pot}}{E_{kin}} = \frac{GMm}{k_B T R} \tag{2.1}$$

The only variable for the kinetic energy in this case is the temperature of the atmosphere. In other words, if the temperature of an atom or molecule increases so that the resulting velocity exceeds the escape velocity of the planet, the atom will escape into space (Seager 2010).

$$\sqrt{\frac{2k_B T}{m}} > \frac{1}{6}\sqrt{\frac{2GM}{R}} \tag{2.2}$$

Since the planet does not undergo major changes in radius or mass anymore at this point, the escape velocity remains constant, and therefore the temperature T has the greatest effect on the escape potential of an atom. There are several mechanisms (subsection 2.2.3)

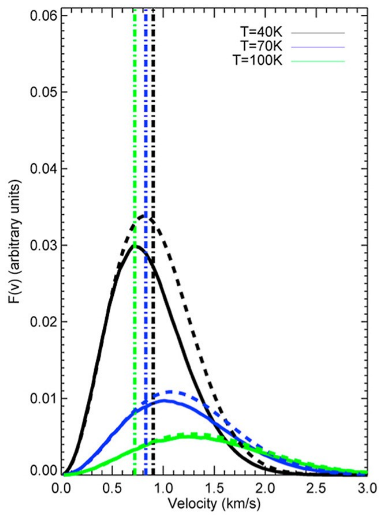

Figure 2.2: Velocity distribution of the atmospheric particles in dependency of the atmospheric temperature. Modified from Chaufray 2021.

that influence the temperature, and therefore, escape processes can be divided into three groups: planetary driven, stellar driven and others. An example of non-stellar driven would be core driven boil off and impact events. However, because the known constraints on exoplanets are much less detailed than those for planets in the Solar System, it is difficult to determine non-stellar driven escape processes. On the other hand, it is less complex to measure the relevant stellar properties and the outer radius and composition of an exoplanet's atmosphere. Stellar high energy radiation is also responsible for driving photo chemistry in a planet's atmosphere. Furthermore, exoplanets that are closer to their host star receive stronger radiation and are more prone to stellar driven atmospheric losses. In this thesis I focus on stellar driven atmospheric heating and escape.

First, we will look at the so-called Jeans escape as it one of the best understood processes which cause mass loss in atmospheres. Because the temperature of an atmosphere in Equation 2.1 is not a fixed value for every particle in the whole atmosphere, but follows a distribution, there will always be particles that are hot and therefore fast enough to exceed the escape velocity of the planet and be lost to space (Catling 2017). Figure 2.2 illustrates this effect as the velocity distribution is shifted towards higher velocities with higher temperatures, whereas the escape velocity remains constant.

Most affected by this process is atomic hydrogen, as it is the lightest possible particle. While the actual mass lost in this way is small, it is a steady loss and affects every planet. As the temperature in the upper atmosphere rises, so does the Jeans escape rate of particles, until it is no longer possible to interpret this process as individual particles being lost, but as a continuous outflow of particles. This second process is called hydrodynamic outflow or blowoff, but there is no clear boundary to the Jeans escape. A good estimate to divide the two is to calculate the loss process as hydrodynamic outflow if the hydrogen loss rate is so high that the hydrogen drags heavier species with it (Catling 2017, Seager 2010). Unlike the Jeans escape, not every planet is affected by hydrodynamic outflow, as the upper atmosphere needs to get quite hot for these processes to occur. In terms of habitability, outflows can play a crucial role in both cases. In a H_2/He dominated atmosphere, like we observe them around the gas giants of our Solar System, it could change the atmosphere so that it is enriched with more complex molecules and therefore more versatile, which should increase the probability of the planet being habitable. Conversely, if we already consider a planet habitable because it has a complex atmosphere, a hydrodynamic outflow could strip away that shell within several Myr to few Gyr, leaving the planet a bare rock. As aforementioned life needs time in a relatable stable environment to develop, a total loss of an atmosphere majorly destabilizes this environment and is therefore, unfavorable for the development of life.

2.2.3 Atmospheric Thermal Processes

The range of thermal processes that affect the temperature of the atmosphere, and therefore the escape rate, is wide and a discussion of all of them is beyond the scope of this work.

The different atmospheric heating and cooling processes that are included in this work are listed below, followed by the assumptions and limitations as described by Johnstone et al. 2018.

Heating

The code used in this work considers five heating mechanisms: stellar X-Rays and ultraviolet radiation (XUV) as well as irradiation in the infrared regime (IR), electron heating, chemical through exothermic reactions and Joule heating. However, the main energy sources are XUV (10-4000 Å) and IR (1-20 µm) radiation. While IR heats the atmosphere directly, XUV acts as an indirect heat source. There are several ways in which XUV can interact with the atmosphere, but in all cases, it starts by interacting with atoms or molecules, which then become ionised or dissociated. At this point, the energy is absorbed by the atmosphere and transformed into heat via shorter or longer detours.

If neutral gas is photo dissociated by the radiation, it will convert this energy directly into heat without any further steps. If the dissociated gas is not neutral, it will store the energy as chemical energy, a state that can also be reached by photo ionisation. As atoms and molecules will always seek a stable, less excited state they will transfer the remaining energy away. This energy either heats up the surrounding atmosphere or is radiated away, which than cools the atmosphere.

Photo ionisation energy can also be transferred to non-thermal electrons, which can then heat other electrons through elastic collisions, or excite neutral atoms and molecules through collisions, which are then transferred into a higher energy state.

Cooling

Cooling occurs when atoms and molecules become excited but are unable to de-excite through mutual energy exchange with other particles. The excess energy is then emitted in the form of IR radiation. In the Kompot code used, this effect is considered for CO_2, H_2O, NO and O. Depending on the species, the code uses different excitation and deexcitation mechanisms and assumptions to achieve a simpler implementation.

CO_2 has its most dominant IR emission feature at 15 μm, and a cool-to-space approximation as presented by Dickinson 1972 is used, which indicates that CO_2 is based on each thermal photon contributing to cooling as it is lost to space. Therefore, not only does each thermal 15 μm photon contribute to cooling, but it can also excite other particles, especially other CO_2 molecules. In addition to this mutual excitation of CO_2 molecules, there is also collisional excitation and excitation by stellar IR radiation. However, the emission of 15 μm photons is the only way CO_2 can cool the upper atmosphere, although it can also be de-excited by collisions. These five processes determine the total excitation and deexcitation rate of CO_2 in the atmosphere.

The wavelengths for these so-called line cooling effects for NO and O are $\lambda_{\mathrm{NO}} = 5.3$ μm (vibrational) and $\lambda_{\mathrm{O}} = 63$ μm and 147 μm, respectively. The specific sources of radiation or collision partners differ from species to species, but the general mechanisms are similar to those described for CO_2. For H_2O the multiple line rotational band in the far IR to microwave region is considered and the only valid excitation mechanism is collision with atomic hydrogen. For further discussion of these cooling mechanisms, see Johnstone et al. 2018.

Conduction

As heating and cooling are not equally efficient at all heights, a steady state would not be possible without some form of energy exchange between different layers. Depending on the species group (neutrals, ions, or electrons) and location, different conduction mechanisms are dominant and therefore more important to consider than less contributing mechanisms.

In the case of neutrals, vortex conduction is most dominant in the lower atmosphere and molecular conduction in the upper atmosphere. To fully calculate the conductivity for each species different species dependent factors are needed. As they are not known in every case, the neutrals used are limited to N_2, O_2, CO_2, CO, O, He, H and Ar.

For ion conduction the process is a little simpler, as the conduction efficiency depends mainly on the atomic mass, the temperature of the ion and the ion conductivity, which can be calculated as described by Banks and Kockarts 1973. There is also no dependence on height, except indirectly through temperature.

The thermal electron gas can be treated very similarly to the ions, with a difference in the calculation of the conductivity (also described by Banks and Kockarts 1973).

Energy Exchange

Heating and cooling are the two main types of energy exchange in the atmosphere, but as mentioned in subsection 2.2.3 there are other ways in which energy can be stored in the atmosphere, and therefore there are more mechanisms by which this energy can be exchanged between particles. In general, energy is exchanged whenever two particles collide. In the case of electron-ion collisions, the Coulomb collision is considered. For neutral ion energy exchanges, the exact process and therefore the amount of energy exchanged depends on the colliding species.

2.3 Co-Evolution of Planets and their Host Stars

The host star has major influence on the evolution of an exoplanet's atmosphere. Furthermore, the host star is the main factor determining how accurately an exoplanet can be observed. The signature of a transiting planet on the photometric and spectroscopic observables of an M dwarf is much greater than that of an F star. This is often referred to as a *small star opportunity* (Benneke et al. 2019).

There are several stellar and orbital characteristics that affect the evolution of a planetary atmosphere. The stellar type is one of the best understood and most influential parameters for discussing planetary atmospheres and habitability as it strongly influences the distance of the habitable zone (Kasting, Whitmire and Reynolds 1993). Furthermore, stars of different types vary strongly in their lifetime, which leads to the assumption that only F, G, K and M stars can provide a stable amount of radiation over a period long enough to allow life as we know. It must also be considered that planets in the habitable zone of K and M stars might be tidally locked (Meadows 2008). The less luminous the star is the closer in is the habitable zone the more probable is tidal locking. For K2-18 b this is probably not yet the case, but it will eventually reach this state (Charnay et al. 2021). Tidal locking leads to a very uneven heating of the atmosphere. Also related to the type of star is the position of the snowline, as mentioned in subsection 2.2.1. Normally, the snowline forms just outside the habitable zone since it is defined as water that is liquid and not yet frozen (Mulders et al. 2015). Another important factor is the activity of the star, especially in the XUV region of the spectrum, which is crucial for atmospheric processes (see subsection 2.2.2 & subsection 2.2.3). The problem is that it is not possible to measure the activity in form of stellar wind and outbursts of most stars directly, as it largely depends on the star's magnetic field. Therefore, the rotation period of the star is used as an estimate since it supports the dynamo of the star. This factor is complicated by the fact that different types of stars behave differently and reach different lifetimes. In general, stars spin up as they approach the main sequence and contract. After the ZAMS they start to spin down due to stellar winds and become less active (Johnstone 2017, Wright et al. 2011, Bouvier et al. 2014). A slower rotating star is less active and the fraction of XUV luminosity evolves over time. For the case studied in this work, it should be noted that M dwarfs such as K2-18 take a special position in stellar evolution, especially in the XUV regime. Even though the total luminosity of the star decreases, the relative amount X-ray and EUV luminosities can remain roughly the same, where as in more massive stars the XUV luminosity declines with the total luminosity. A comparison to highlight this effect can be seen by looking at GJ 176: a M2.5V star has an EUV ratio of $\log(F_{\mathrm{EUV}}/F_{\mathrm{bol}}) = -3.75$, whereas G2V stars are around $\log(F_{\mathrm{EUV}}/F_{\mathrm{bol}}) = -5.78$ (Sreejith et al. 2020). Another important factor is that M dwarfs evolve much more slowly than other stars. A solar-like star rotates down within about half a Gyr, after which they follow a period-mass relationship. For M dwarfs the stellar mass is not a clear indicator for the rotational period within this time. A study of $\sim 8,500$ M2 dwarfs by West et al. 2008 shows that the expected activity time is 1.2 Gyr $\pm\, 0.4$. The activity of the stars has been followed by spectroscopic analysis of potential Hα emissions.

This chapter summarizes the relevant parts of the formation history of planets and especailly their atmospheres, in particular the fact that the composition of primordial atmospheres is almost identical to that of the protostar. If observations suggest that this is not the case, the planet is most likely surrounded by a primary or secondary envelope. Combining this knowledge with the strong influence of the host star on the atmospheric processes and evolution, we can now look at the actual data from the studied exoplanet K2-18 b. In this work I provide estimates on the current and short-term evolution of K2-18 b's atmosphere due to the host star. Since stellar XUV could be much higher during the early year of the planetary system, the actual loss mechanisms could be even more dominant. The following chapter will not only present the current state of knowledge of K2-18 b's atmosphere but will also attempt to classify the planet and its atmosphere in the schemes presented. It will also give an outlook on what the simulation might be able to constrain in detail.

3 Observation of K2-18 b: Current State-of-the-Art

In order to give the reader a better understanding of the K2-18 system this chapter describes the current data sets and the constraints that can be placed on the nature of K2-18 b, its atmosphere, and host star based on prior knowledge gained from observations. It includes multiple results obtained by Benneke et al. 2017, Benneke et al. 2019 and Tsiaras et al. 2019 using Hubble Space Telescope (HST) observations taken by the wide field camera 3 (WFC3). Furthermore, a discussion on the stellar high-energy spectrum as modelled by France et al. 2016 is also included.

3.1 Classification of K2-18 b

In the following, K2-18 b will be classified according to the schemes presented in chapter chapter 2. As mentioned before, to classify a planet, its mass and radius, or density, must be taken into account. Smaller, more dense planets are considered rocky, while larger, looser planets are considered gaseous. This classification also determines whether K2-18 b should be considered a super-Earth or a mini-Neptune. This thesis follows the definition of Wordsworth and Kreidberg 2022, which classifies a planet as *rocky* if its density is between that of pure iron and pure $MgSiO_3$, which are the core and mantle material of most rocky planets. The mass of K2-18 b is $M_{\mathrm{K2-18b}} = 8.63 \pm 1.35\ M_{\oplus}$ according to Cloutier et al. 2019; the radius and density are taken from Benneke et al. 2019 and are considered to be $R_{\mathrm{K2-18b}} = 2.610 \pm 0.087\ R_{\oplus}$ and $\rho_{\mathrm{K2-18b}} = 2.67^{+0.52}_{-0.47}$ g cm^{-3}. The most compact scenario allowed by the data within 1 σ is $\rho_{\mathrm{max}} = 3.19\ g\ cm^{-3}$, which is the density of $MgSiO_3$. Hence, it is possible that K2-18 b is rocky or gaseous, but a definite classification is not possible, due to a low confidence level.

Even though I simulated multiple scenarios which cover both possibilities, a rocky nature of K2-18 b with a thin atmosphere and also a very extended envelope, K2-18 b will be referred to as a *Sub-Neptune* in this thesis due to its clear tendency towards the density of a gaseous planet. The classification of the atmosphere of K2-18 b is also unclear, as it depends largely on the amount of H_2O and other gases. If the H_2O content is at the lower end of the range presented later on, it would still be possible for K2-18 b to be surrounded by its primordial atmosphere. However, a H_2O content higher than that of the star would indicate a primary or secondary atmosphere (see subsection 2.2.1). The H_2O content of a star is largely determined by the amount of oxygen in the protostar nebula, the remnants of which later become the protoplanetary disc.

3.2 Known Constraints on K2-18 b

First discovered by Montet et al. 2015, K2-18 b quickly became one of the most well known and well studied habitable zone transitional exoplanets today. Although the amount of actual data obtained by Benneke et al. 2017, Benneke et al. 2019 and Tsiaras et al. 2019 with *WFC3* from HST, as well as Spitzer and Kepler not cover a wide spectral range, researcher has revised and analysed this data many times with different approaches. The interest in K2-18 b can be explained with the nature of its system, M dwarfs such like K2-18 are the least luminous in the optical range, some of the most reddest, and smallest main sequence stars, which allows for a much easier detection and characterization in the infrared regime, due to better contrast between star and planet. Additionally K2-18 b orbits within the habitable zone of its host star, which leads to an equilibrium temperature of $T_{\mathrm{eq}} = 254.9 \pm 3.9$ K as determined by Benneke et al. 2019 assuming a bond albedo $A = 0.3$, which is quite similar to Earth with $T_{\mathrm{eq}} \simeq 257$ K. The short orbital period has also several advantages for observational astronomy. Benneke et al. 2019 measured an orbital period of $P_{\mathrm{planet}} = 32.9$ days (0.159 AU), which allows for many observations in a relatively brief period.

With a mass of $M_{\mathrm{K2-18b}} = 8.63 \pm 1.35\ M_{\oplus}$ (Cloutier et al. 2019) and a radius$R_{\mathrm{K2-18b}} = 2.610 \pm 0.087\ R_{\oplus}$ (Benneke et al. 2019) this exoplanet lies above the so called *radius valley*, which was first described by Fulton et al. 2017. In general exoplanets above the radius valley are considered to be more likely of a gaseous nature and the ones below are more likely to be rocky. But the classification of K2-18 b is still unknown, some classify it as a super-Earth (Benneke et al. 2017, Madhusudhan et al. 2020), others see it as a sub-Neptune (Benneke et al. 2019,Charnay et al. 2020). This ambiguity and several scenarios of the compositions of the core and the atmosphere will be discussed in the following. Already the total mass of the atmosphere is not entirely clear, but was determined to be $\lesssim 5$ % by Madhusudhan et al. 2020. The maximum mass of the atmosphere of K2-18 b within 1σ is therefore $0.5988\ M_{\oplus}$ or $3.576 \cdot 10^{24} kg$, which is smaller than the actual uncertainty in the total mass of the planet. Other scenarios proposed by Madhusudhan et al. 2020 also include much smaller mass fractions of 0.006% ($= 0.518 \cdot 10^{-3}\ M_{\oplus}$) or 0.03% ($= 2.589 \cdot 10^{-3}\ M_{\oplus}$) for different scenarios of core and atmospheric composition.

3.2.1 Atmospheric Composition

The atmosphere of K2-18 b is a highly discussed topic in exoplanetary science, seeing as the atmosphere of a planet strongly influences its habitability. In the following, I will comprehend the current results of recent research. It covers multiple scenarios of the chemical composition of the atmosphere as well as the potential existence and nature of clouds.

Three different groups studied this exoplanet using observational data. Benneke et al. 2017 and Benneke et al. 2019 observed twelve transits of K2-18 b covering thirteen different wavelength channels. In addition to 9 channels of *WFC3* covering a range from 1.12 μm

to 1.63 μm, two channels of *IRAC*/Spitzer covering wavelengths between 3.15 μm and 5.02 μm and one observation by Kepler as part of the K2 survey in a band from 0.43 μm to 0.89 μm. This data is shown in Figure 3.1. Tsiaras et al. 2019 only observed data with HST/*WFC3* but used seventeen different channels covering the range from 1.139 μm to 1.620 μm.

The exact abundances of the gases that make up the atmosphere of K2-18 b are the subject of recent studies, but the main components are known to be H_2 and He (Benneke et al. 2019, Tsiaras et al. 2019 and Madhusudhan et al. 2020). The volume mixing ratio (VMR) of the various components, as well as the existence of trace gases, is currently unknown. But many studies suggest the existence of H_2O in some form, the exact amount of which has yet to be determined. Current values, depending on studies and scenarios, range from $\log(X_{\mathrm{H_2O}}) = -3.62$ to -0.30 (0.02% to 50%), as determined by Madhusudhan et al. 2020, Benneke et al. 2019 and Tsiaras et al. 2019. While it should be noted that only Tsiaras et al. 2019 reached values in the order of 50% in one case, the maximum values determined by Benneke et al. 2019 ($\log(X_{\mathrm{H_20}}) = -1.05$) and Madhusudhan et al. 2020 ($\log(X_{\mathrm{H_20}}) = -0.99$) and the other prospected scenarios of Tsiaras et al. 2019 ($\log(X_{\mathrm{H_20}}) = -0.90$) are much lower. While the lowest could still be argued to be consistent with the $\log(X_{\mathrm{H_20}}) = -4.0$ of a primordial atmosphere (see subsection 2.2.1, Gaidos 2017, Molyarova et al. 2017), all other values indicate a primary or secondary atmosphere, although the amount of hydrogen and helium is still high. The assumption of the existence of H_2O in the atmosphere is based on the clear presence of a spectral line at 1.4 μm, which may be caused by the H_2O vapour vibrational band, which is well covered by the HST data, as shown in Figure 3.1.

In addition, there are several other trace gases that are discussed as being abundant in the atmosphere of K2-18 b. In most cases, these trace gases are *allowed* but not *necessary*, which means that they neither improve nor worsen the fit of the models significantly. H_2O, on the other hand, is considered necessary for a good fit. In Table 3.1 the different suggested trace gases are listed.

The confidence levels for the detection of different gases, especially H_2O, vary based on method. The analysis carried out by Benneke et al. 2019 only lists a best fit value with uncertainties for H_2O. Fot the other species only the maximum possible abundance within 2 σ is listed. Madhusudhan et al. 2020 simulated five scenarios, including a full model with inhomogeneous clouds and haze, a clear atmosphere, an opaque cloud deck, an inhomogeneous cloud layer, and a scenario where the existence of H_2O was forbidden. For each scenario and species Madhusudhan et al. 2020 listed best fit values and upper and lower uncertainty levels. In Table 3.1 only two scenarios are shown, the cases not shown are consistent with the full model within 1 σ for each value. The strong dependence on the abundance of H_2O of the retrieval models can be seen particularly well by comparing the abundance of CH_4 for the two cases shown by Madhusudhan et al. 2020.

A alternative interpretation of the peak at 1.4 μm is proposed by Bézard, Charnay and Blain 2020. In their comment on the results from Tsiaras et al. 2019 the authors compared three different cases for the peak. The cases are absorption profiles of H_2O only, of CH_4 only, and of H_2O and CH_4 combined. They find that the effect of CH_4 on the

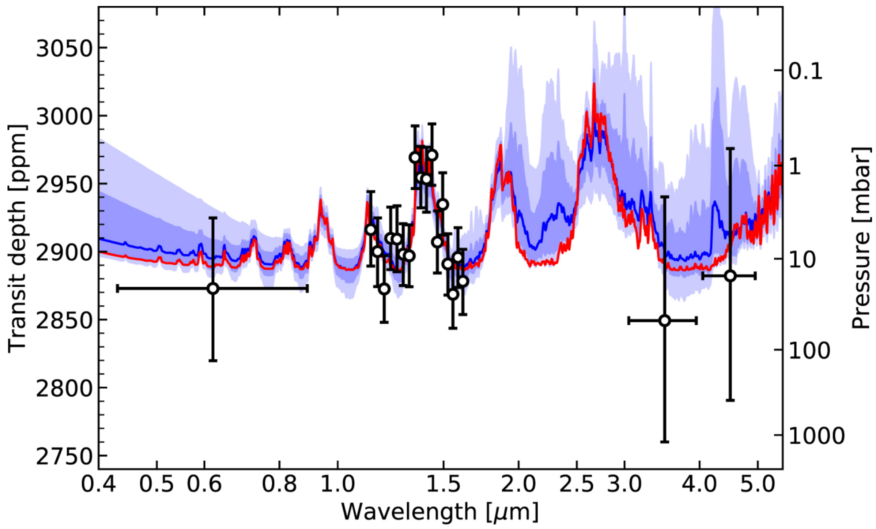

Figure 3.1: Spectral data as obtained by Benneke et al. 2019. Kepler/K2 data on the short wavelength side, *WFC3*/HST data in the middle and two channels of *IRAC*/Spitzer data on the long wavelength side. The peak covered by the HST data is related to the 1.4 μm line of the H_2O vapour vibrational band. The red line is the best fit model to the data. Figure taken from Benneke et al. 2019.

total absorption is greater than that of H_2O. They therefore question whether the 1.4 μm line is indeed a clear indicator of H_2O in the atmosphere. It is also stated that additional data in the range of $1.6 - 3.7$ μm should be obtained for a clear distinguish between the abundance of H_2O and CH_4. JWST's *NIRSpec* covers a wavelength range of $0.6 - 5.3$ μm, which is needed to make this distinction (Rigby et al. 2022). The ambiguous peak at 1.4 μm which may be caused by H_2O or by CH_4 also explains the significant difference between the two models of Madhusudhan et al. 2020, as shown in Table 3.1.

Due to proposals by Hu and Damiano 2021 and Madhusudhan et al. 2021 K2-18 b is now part of cycle 1 of the JWST observations. The schedule covers almost a full year between January 2023 and January 2024 with a total of nine transits. During the measurements *NIRSpec*, *NIRISS* and *MIRI* will be used with observation times between 6.89 hours and 11.35 hours. However, as this data will not be released until 2024, it cannot be considered for this thesis.

3.2.2 Clouds

Like the composition of the atmosphere, the existence of clouds is currently not strongly constrained. The models of Benneke et al. 2019 favour clouds, while Madhusudhan et al. 2020 don't find strong evidence for clouds in the atmosphere of K2-18 b.

Benneke et al. 2019 favour the existence of clouds because otherwise their models would need excessive amounts of H_2O in the atmosphere to be consistent. It is important to

species	abundance [log(X)]	reference	additional comments
CH_4	-2.61	Benneke et al. 2019	2σ maximum
	$-8.20^{+2.53}_{-2.34}$	Madhusudhan et al. 2020	full model
	$-1.11^{+0.53}_{-1.22}$	Madhusudhan et al. 2020	no H_2O
CO	-1.12	Benneke et al. 2019	2σ maximum
CO_2	-1.62	Benneke et al. 2019	2σ maximum
NH_3	-0.87	Benneke et al. 2019	2σ maximum
	$-8.64^{+2.15}_{-2.06}$	Madhusudhan et al. 2020	full model
	$-7.27^{+2.91}_{-2.92}$	Madhusudhan et al. 2020	no H_2O
N_2	-0.96	Benneke et al. 2019	2σ maximum

Table 3.1: Different trace gas abundances from different studies and models. The values from Benneke et al. 2019 are the maximum values within 2 σ allowed by the simulation. Madhusudhan et al. 2020 ran a total of five models, two of which are shown here, a full model with inhomogeneous clouds and haze, and a model that explicitly excluded H_2O as a possible species in the atmosphere. Comparing the CH_4 abundances in the two cases simulated by Madhusudhan et al. 2020 it is clear that the presence of H_2O and CH_4 are co-dependent. As an indication of atmospheric classification, these trace gases behave similarly to H_2O, the lowest possible abundances are still consistent with a primordial atmosphere accreted from the proto planetary disc as in Molyarova et al. 2017, the highest values would indicate a more complex atmosphere, which could not have been accreted from the proto planetary disc.

mention that the models by Benneke et al. 2019 also support a H_2O abundance between $\log(X_{H_2O}) = -2.08^{+1.03}_{-1.39}$ in the form of H_2O vapour. Considering the atmospheric temperature and the incoming irradiation of the host star and the resulting equilibrium temperature of 255 K, it is possible that the clouds are actually made up of liquid H_2O or H_2O ice. The top pressure for these clouds was determined to be $\log(P_{\text{cloudtop}}) = 1.37^{+0.77}_{-0.48}$ mbar.

In contrast, Madhusudhan et al. 2020 state that they find no convincing evidence for clouds. But the preference for clouds over a cloudless scenario could easily be due to a statistical error, as it only reaches 1.2 σ. Even if K2-18 b was partially covered by clouds, their models are not able to place strong constraints on the clouds, i.e., the cloud top pressure would vary between $\log(P_{\text{cloudtop}}) = -1.0$ and 3.3 mbar.

Tsiaras et al. 2019 assume a thick grey cloud deck and predict an even higher cloud top pressure of $\log(P_{\text{cloudtop}}) = 4.47^{+0.35}_{-0.32}$ mbar. But they also mentioned that in view of the poor data situation it is hardly possible to get reasonable constraints.

The question of the existence of clouds will most likely remain unresolved unless further studies with better models or additional data are included. Benneke and Seager 2013 for example suggest by stacking 10-20 transit observations, it is possible to distinguish between a mini-Neptune type with a cloud-free H_2 dominated atmosphere and a more volatile and aerosol rich atmosphere surrounding a rocky planet.

3.3 Stellar Properties

To further close in on the actual appearance of K2-18 b, the following section will discuss the influence of stellar radiation on the atmosphere of planets. As mentioned in section 2.3, the host star has a major influence on the evolutionary path of the exoplanet's atmosphere. It is therefore particularly important to obtain a suitable spectrum for simulations using the Kompot code. Particular emphasis should be placed on the coverage of the lower wavelengths in the X-ray and UV regime, as these have a significant impact on atmospheric processes such as atmospheric heating, photochemistry, and mass loss, etc. (Johnstone 2017). As there is no spectrum of K2-18 covering X-rays and UV radiation yet, a star as similar as possible to K2-18 with an existing spectrum was used. For this purpose, GJ176 was used as a substitute, due to the similarity between GJ176 and K2-18 in terms of their stellar parameters, listed in Table 3.2. Besides the stellar type and temperature, especially the rotational period P_{rot} is important as an estimate of the stellar activity. Since West et al. 2008 found that most M dwarfs become inactive within 2.0 Gyr (σ), it can be assumed that both GJ176 and K2-18 are relatively inactive stars.2

Parameter	GJ176	K2-18
Type	M2.5V[1]	M2.5V[2]
T_{eff} [K]	3680	3506
P_{rot} [days]	38.92 ± 0.00	33.62 ± 15.65
Metallicity [Fe/H]	0.14	0.09
Age [Gyr]	5.60 ± 0.9	4.00 ± 2.34

Table 3.2: Parameters of GJ176 and K2-18. All values are taken from Gaidos et al. 2023, if not marked otherwise.

The GJ176 spectrum used here is taken from the MUSCLES survey. The MUSCLES survey provides semi-empirical spectra for several M dwarfs down to 5Å = 2.48 keV, including GJ176 (France et al. 2016; Youngblood et al. 2016; Loyd et al. 2016, version 2.2 is used here) To further justify the use of GJ176 as a K2-18 analogue, the MUSCLES spectrum of GJ176 and a synthetic spectrum of K2-18 are shown in Figure 3.2. The synthetic spectra of K2-18 were produced by Christie et al. 2022 based on the PHOENIX BT-Settl model as described by Allard, Homeier and Freytag 2012 and do not cover the low wavelength regimes relevant to the simulations. Therefore, an overlap region is shown which is covered by both spectra. It is clear that GJ176 provides the best available proxy for K2-18 at the moment. The actual relevant part to the Kompot code – the XUV regime – is shown in Figure 3.3.

[1]von Braun et al. 2014
[2]Schweitzer et al. 2019

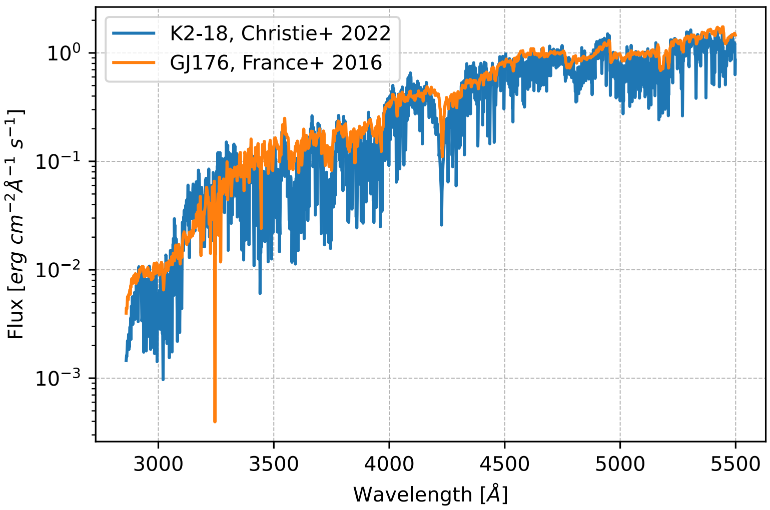

Figure 3.2: Comparison of the spectrum of GJ176 by the MUSCLES survey and the artificial spectrum of K2-18 created by the CAMEMBERT project, based on the PHOENIX BT-Settl model (Allard, Homeier and Freytag 2012)

.

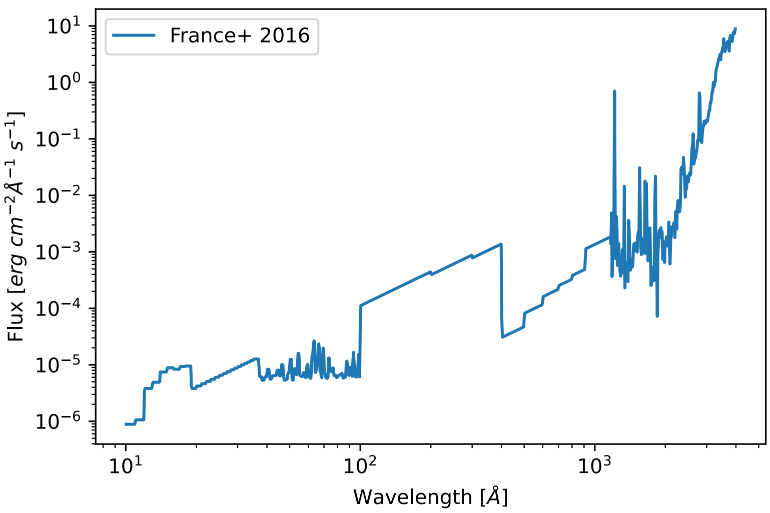

Figure 3.3: XUV part of the spectrum of GJ176 as used by the Kompot code. Data from the MUSCELS survey (France et al. 2016; Youngblood et al. 2016; Loyd et al. 2016).

.

4 Model Description and Simulation Setup

In the following sections I will present the main algorithm of the Kompot code, followed by a a description of tje simulation setup. For further details about the Kompot code, such as the numerical solvers used, can be found in the paper by Johnstone et al. 2018. The results of these simulations are presented and discussed in chapter 5.

4.1 The Kompot Code

The Kompot code, which was originally developed by Johnstone et al. 2018, simulates the thermal and chemical structure of atmospheres in 1D, calculates the thermal atmospheric loss, and is written in Fortran and Python. It considers multiple heating mechanisms (see chapter 2) and over 500 chemical reactions, including photochemical reactions. The species included cover a wide variety of combinations of elements like N, O, C, H, and He. Energy sources, which are taken into account, are XUV (X-Rays and UV radiation) and IR radiation. The domain of the simulations is realised by a finite static linear grid of cells of adjustable size. The cells are resized by a a so called *stretch factor*. The *strecht factor* is defined as the ratio of the size of the lowermost cell to the last cell at the exobase. By default, an offset of fifty cells is used before stretching. Each calculation is made for the centre of each cell. To prevent the code from crashing due to the absence of ions, there is a chemical pre-evolution of 100 s. This pre-evolution time is skipped if the simulation is started from a *restart file* from a previous simulation. The size of the time step is determined by multiplying the time it takes for a sound wave to travel through a cell by the Courant number $\mathcal{C}$, which in most cases is about 1 to make the code numerically more stable. The code then performs the operations in each step in the following order, unless otherwise specified. It starts by updating the spectrum of the XUV and IR radiation, as well as the impact of the non-thermal electrons. This is done every hundred steps and is assumed to be constant for the rest of the time. Afterwards, it calculates the hydrodynamics, such as escape processes (see subsection 2.2.2). Then it runs the chemical network, again only every hundred steps. As Johnstone et al. 2018 has shown, this greatly reduces the runtime, but hardly affects the overall accuracy of the simulation. The next step is to determine the temperature of each cell by combine the heating and cooling processes mentioned in subsection 2.2.3, followed by a calculation of the energy exchange between the cells, as well as various conduction and diffusion processes (see subsubsection 2.2.3). In the last step, the new exobase height is calculated if a dynamic or semi-static case had been chosen. This is done until a steady state is flagged by the code and the simulation is terminated by hand.

Another important concept to consider for atmospheric loss is the correct definition of the exobase. In the Kompot code, the exobase is defined as the point where the mean free path length begins to exceed the scale height of the atmosphere (Johnstone et al. 2018). It should be noted that the Kompot code was originally written for Earth or Venus-like atmospheres, i.e., atmospheres composed of species heavier than hydrogen and helium, so this definition may not be ideal for hydrogen-dominated atmospheres. In any case, the maximum possible limit would be the Roche limit, which defines the point at which a larger and more massive body, such as a star, would tear apart a smaller body, such as a planet, if it expanded beyond that limit. If only the atmosphere expands beyond this limit, the core of the planet may not be affected, but the atmosphere would certainly be lost (Carroll 2017). To calculate the Roche limit, the following estimate from Carroll 2017 is used:

$$r \simeq 2.456 \cdot (\frac{\overline{\rho_*}}{\overline{\rho_P}})^{\frac{1}{3}} \cdot R_* \tag{4.1}$$

Where $\overline{\rho}$ are the mean densities of the planet and star, and R_* is the radius of K2-18.

At the start of the simulation, the grid on which the atmosphere is allowed to expand, and contract must be defined. Ideally, one would choose a grid that does not impose artificial constraints on the simulation. For Earth and Venus-like planets, this is not a problem, as these atmospheres tend not to undergo significant changes in the size of the atmosphere. For hydrogen dominated atmospheres the situation is different, as hydrogen will always try to expand due to its low mass. The upper limit of how far the atmosphere can physically expand before it is no longer bound to the planet is the Roche Limit. According to Equation 4.1, the height of this limit for K2-18 b is $1.051 \cdot 10^6$ km[1]. Unfortunately, a grid with this upper limit will either have errors depending on the exact configuration or will take too long for one iteration so it stops itself. Reducing this upper limit by an order of magnitude solves the configuration problems, but results in exorbitant runtimes on the CPU node used. Therefore, either a lot of time is needed to run such a simulation, or the code must be modified to run on either multiple CPUs or a GPU, which would speed up the simulations. To illustrate the effect of this kind of artificial constraint I have to place on my simulations, I have run simulations with different upper domain limits. The effects will be discussed in chapter 5.

4.2 Simulations of K2-18 b

In order to test the setup, a number of well-studied cases (e.g., current Earth, pure water atmosphere) were run and the output compared with existing results, for example from the paper by Johnstone et al. 2018. Once the results were satisfying, the following simulations for K2-18 b were conducted.

[1]The actual physical limit for the atmosphere may be lower but is difficult to estimate.

4.2.1 Case I: Hydrogen-Helium Atmosphere

For the first scenario a relatively simple case was chosen to make sure the grid configuration was working with the planetary and stellar parameters. The stellar spectrum was taken from GJ176 as described in chapter 3. The planetary parameters are the actual mass (8.63 $M_\oplus$), radius (2.61 $R_\oplus$) and semi-major axis (0.159 AU). To create a simple baseline for all the other simulations, the complexity of the atmosphere is reduced by including only H_2 and He in a volume mixing ratio of 80 % hydrogen and 20 % helium. The values are based on the composition of Neptune (Lissauer and Pater 2013, Table E.13), because the exact composition of sub-Neptunes is unknown (Bean, Raymond and Owen 2021). To keep it as simple as possible I used unified temperatures instead if separated temperatures. Separated temperatures in this case would indicate that each group of species, i.e., neutrals, ions, and electrons, would have their own temperature. The simulation was terminated at a domain time of 2.85 days after the code indicated a stable solution.

4.2.2 Case II: Hydrogen, Helium, Water

As a follow-up to my previous simulation, I wanted to make the atmosphere more complex and closer to what is constrained by observations (see chapter 3). I added H_2O as it is the species upon which the most publications can agree. For a complete picture it would be necessary to also add CH_4 to the atmosphere as the Kompot code is not yet capable to simulate CH_4 I was not able to include it in my thesis, but it needs to be kept in mind for future studies. In total I started to simulate seven different cases that lie between $\log(X_{H_2O}) = -0.82$ (15 %) and $\log(X_{H_2O}) = -3.70$ (0. 002%), since these two are the limits[2] found by Benneke et al. 2019, Tsiaras et al. 2019 and Madhusudhan et al. 2020.

To avoid numerical chaos, I started all simulations at 1 AU with separated temperatures. Separated temperatures in this case means that each group of species, i.e., neutrals, ions, and electrons, has its own temperature unlike in the case of the hydrogen-helium-only atmosphere. For the upper limit of the volume mixing ratio of $\log(X_{H_2O}) = -0.82$ I used $\log(X_{H_2}) = -0.15$ and $\log(X_{He}) = -0.82$. For the cases $\log(X_{H_2O}) = -1.30$, -1.70, -2.00, -2.30, -2.70 and the lower limit of -3.70 I chose $\log(X_{H_2}) = -0.10$ and adjusted the amount of helium to get $\log(X_{tot}) = 0.00$. To further stabilise the simulation, I added a small amount of O_2 ($\log(X_{O_2}) \ll -3.70$) at the beginning. All the aforementioned cases contain at least $\log(X_{H_2}) = -0.15$ and $\log(X_{He}) = -0.82$, inspired by the composition of Neptune mentioned above. For each case, I simulated until it reached a stable state and then moved it further inwards in three steps, 0.5 AU, 0.25 AU and 0.159 AU, the actual semi-major axis of K2-18 b around its host star. After the simulations were marked as stabilised by the code, there was still very little evolution visible in some cases. Also, the originally separated temperatures were no longer separated for the whole simulation, which was restarted at 0.159 AU, but were identical down to 0.01 K. I decided to investigate this trend further and post-processed the results of these simulations by restarting them without separated temperatures, as it makes no difference according to the results. Merging the temperatures also allowed for the code to run faster. I also

[2]The one scenario proposed by Tsiaras et al. 2019, which would contain 50 % water, was neglected.

restarted each case twice, once with the upper limit for the exobase expansion held at 6,000km, and once set it to 7,000km. In all cases the atmosphere immediately inflated to 7,000km. This test was done because 6,000km (and also 7,000km) are arbitrary limits and it is necessary to investigate the influence of this artificial constraint.

4.2.3 Determining the Simulation Speed

Additionally I ran simulations to determine the effect of the number of bins in the XUV part of the spectrum used on the speed and accuracy of the code. There are six cases with different numbers of bins for two different water contents (1 % and 0.5 %). These were both set to 1 AU to avoid chaotic behaviour due to too large a radiation effect. I chose six bin numbers between 10 and 1,000 bins for each water content with 1,000 bins being the default. The spectrum of GJ176 with the different bin numbers is shown in Figure 4.1.

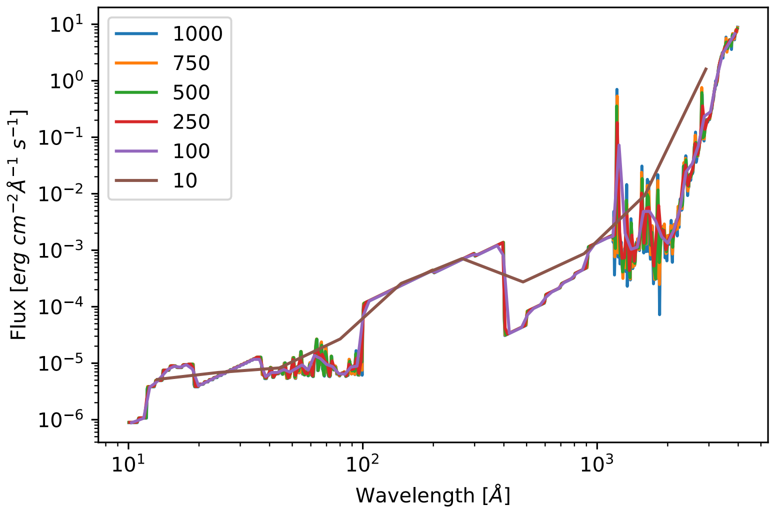

Figure 4.1: XUV spectrum of GJ176 as in Figure 3.3 with different bin number, which were investigated in their impact on speed and accuracy of the simulations. It can be seen that especially the 10 bin spectrum tend to overestimate the flux in some regions.

5 Results and Discussion

This chapter will present the results for the different scenarios and discuss them with a focus on atmospheric lifetime. It starts with the base line case containing only hydrogen and helium. Afterwards, it will have a look at the more complex cases with multiple water contents, where two pressure profiles are discussed as well. Finally, it will cover the speed analysis and what we can learn from it for future work.

5.1 Case I: Hydrogen-Helium Atmosphere

The results show significant changes in the atmosphere over the course of the simulated time of roughly 3 days. While H_2 always dominates the exobase with nearly 100 %, the abundance of H increases drastically during this time. It starts at about 10^{-4} % and reaches 0.068 % in the last step. The third, most abundant species are H+ and electrons, each accounting for $0.186 \cdot 10^{-3}$ %. The altitude-abundance profile of the three hydrogen species is shown in Figure 5.1. This is particularly relevant because the lighter atomic or ionic hydrogen is much easier to lose to space than molecular hydrogen. The three dominant mass loss rates caused by Jeans escape as calculated by the Kompot code are listed in Table 5.2. The output of this first simulation can also show why the processes in

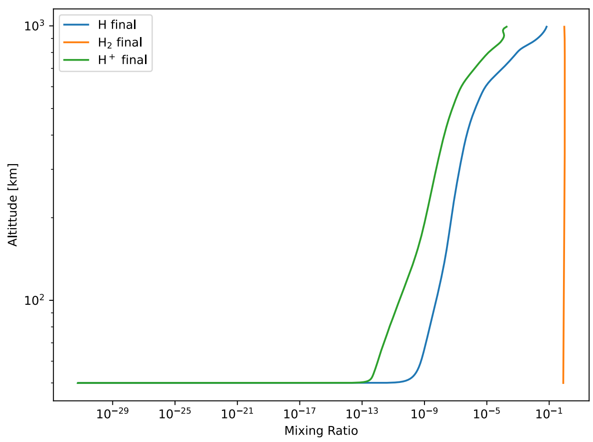

Figure 5.1: Species profile of the pure hydrogen-helium atmosphere.

the upper atmosphere are especially relevant to the evolution. In Figure 5.2 the heating and cooling at the beginning and the end of the simulation are plotted. While heating and cooling are not equal in the beginning at the exobase, they are identical in the end, which then provides a stable temperature in the upper atmosphere, it can be seen that below $\sim 5 \cdot 10^3$ km both become small. Therefore, there are no more significant changes below this altitude because heating by any heat source is the most relevant cause for any process in the atmosphere. This is also visible in Figure 5.3 and Figure 5.4, which show a

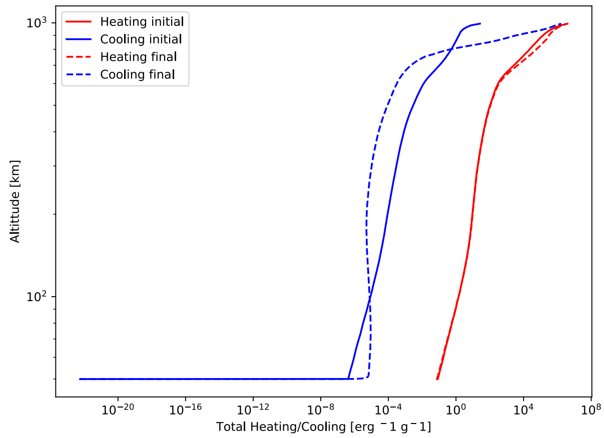

Figure 5.2: Total heating a cooling profiles of the hydrogen-helium atmosphere. Initial state in solid lines and final state in dashed lines. It can be seen that heating and cooling in the upper atmosphere are different in the beginning, but identical at the end. This means the upper atmosphere has reached a stable temperature.

pressure-temperature profile, respectively an altitude-pressure profile, from the start and the end of the simulation. The only significant temperature and pressure changes happen above $\sim 5 \cdot 10^3$ km.

species	Jeans mass loss rate [$g\ s^{-1}$]
H	$0.126 \cdot 10^7$
H^+	$0.345 \cdot 10^4$
H_2	$0.196 \cdot 10^2$

Table 5.1: Three most dominant Jeans escape mass loss rates for the simulation of K2-18 b with a Hydrogen-Helium atmosphere.

Atomic hydrogen is clearly the dominant species lost to space. To better understand the impact of the mass loss rate of 0.12610^7 g s-1, I have calculated the lifetime of the atmosphere for different planetary properties as described by Madhusudhan et al. 2020[1].

[1]A more detailed describtion of these scenarios can be found in chapter 3. For here it is enough to

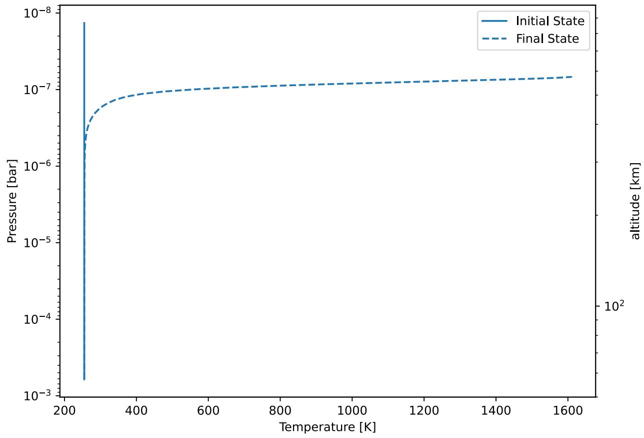

Figure 5.3: Pressure-Temperature profile of the pure hydrogen-helium atmosphere. It is clear that the only significant change in temperature happens above $\sim 5 \cdot 10^3$ km, resp. below 10^{-6} bar.

By dividing the atmospheric mass by the mass loss rate of hydrogen I obtained the estimated lifetime of these atmospheric scenarios, which are listed in Table 5.2 and all of them exceed the lifetime of the universe and therefore, should be considered stable.

atmospheric mass fraction [%]	lifetime [Gyr]
5.0	$64,858$
0.03	389
0.006	78

Table 5.2: Lifetime of the three scenarios and atmospheric mass fractions as proposed by Madhusudhan et al. 2020. All of them exceed the lifetime of the universe.

5.2 Case II: Hydrogen, Helium, Water

The follow-up cases contain different amounts of water between $\log(X_{H_2O}) = -0.82$ (15 %) and -3.70 (0.02 %). Before discussing the loss rates of the different scenarios, the temperature will be considered, as it causes the loss or more precisely the heating and cooling.

remember that there are three different atmospheric mass fraction, i.e. 5 %, 0.03 %, and 0.006 %.

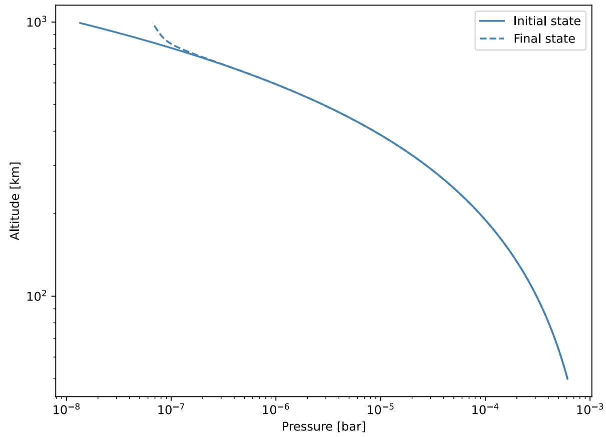

Figure 5.4: Altitude-Pressure profile of the pure hydrogen-helium atmosphere. It is clear that the only significant change in pressure happens above $\sim 5 \cdot 10^3$ km.

5.2.1 Atmospheric Properties

In Figure 5.5 the total heating and cooling is plotted against the altitude. At the start [2] of the simulation the heating dominates over the whole simulation domain. There are two peaks in the heating, one at $\sim 2 \cdot 10^2$ km and one above 10^3 km, but the latter one reaches much higher heating rates up to 10^6 erg s^{-1} g^{-1}.

The other major factor which influences the loss rate is the mixing ratio at the exobase, these values are shown in Table 5.7 and Table 5.8. The three most dominant species account for more than 99.7 % of the total upper atmosphere's volume mixing ratio and are depicted exemplary in Figure 5.6. In all cases the profiles look similar with an almost equal amount of H and H_2 at the exobase and then going towards a clear H_2 dominance below $\sim 2 \cdot 10^3$ km. The mixing ratios are needed to avoid overestimating the total loss. For example, H^+ has relatively high loss rates compared to H_2 but is much less abundant at the exobase. Simply adding up the mass loss rates would therefore overestimate the true total loss, as H^+ would be lost quite quickly and therefore contribute much less to the total mass loss in the long term.

5.2.2 Atmospheric Loss Rates

The loss rates for these different scenarios are listed in Table 5.5 for 6,000km and in Table 5.6 for 7,000km. The cases marked with ★ are post-processed, i.e. they were restarted as they still showed small changes even though the Kompot code claimed they were stable. This post-processing was done twice, once with the exobase limited to 6,000 km and once with the exobase limited to 7,000 km.

[2]Start in this case means the restart of the simulation at 0.159 AU after the temperatures were merged.

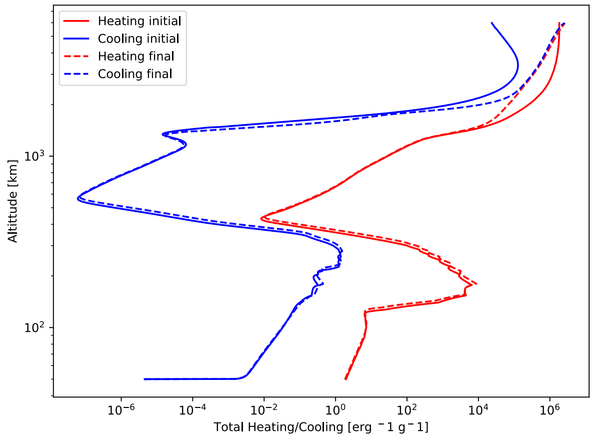

Figure 5.5: Total heating a cooling profiles of case with, $\log(X_{H_2}) = -0.82$ and the exobase limited to 6,000 km. Initial state in solid lines and final state in dashed lines. It can be seen that heating and cooling in the upper atmosphere are different in the beginning, but identical at the end. This means the upper atmosphere has reached a stable temperature.

$\log(X_{H_2O})$	$\log(X_H)$	$\log(X_{H_2})$	$\log(X_{H^+})$	$\log(X_{total})$
$-0.82^\star$	-0.2779	-0.3300	-2.6536	-0.0009
-1.30	N/A	N/A	N/A	N/A
$-1.70^\star$	-0.3024	-0.3036	-2.6307	-0.0013
$-2.00^\star$	-0.2876	-0.3191	-2.6533	-0.0010
$-2.30^\star$	-0.2891	-0.3177	-2.6091	-0.0011
$-2.70^\star$	-0.2870	-0.3199	-2.6162	-0.0011
$-3.70^\star$	-0.2900	-0.3170	-2.6073	-0.0011

Table 5.3: Three most dominant species at the exobase of 6,000 km for multiple water content scenarios at the end of a stable simualtion. These three species make up at least 99.7 % of the volume mixing ratio. Therefore, the other species are considered irrelevant to the overall process as they also have small loss rates. Simulations marked with $\star$ are post-processed because they showed a small evolution even though the code claimed they were stable. The run with $\log(X_{H_2O}) = -1.30$ unfortunately did not finish in time.

Simply adding up the loss rates would overestimate the total loss, due to different abundances as aforementioned. To avoid this kind of overestimation, all loss factors have been weighted by their volume mixing ratio and then summed up. The results are shown in Table 5.5 and Table 5.6. The time it would take to lose the mass equivalent of one atmosphere at each loss rate is also given in these tables for all the scenarios described

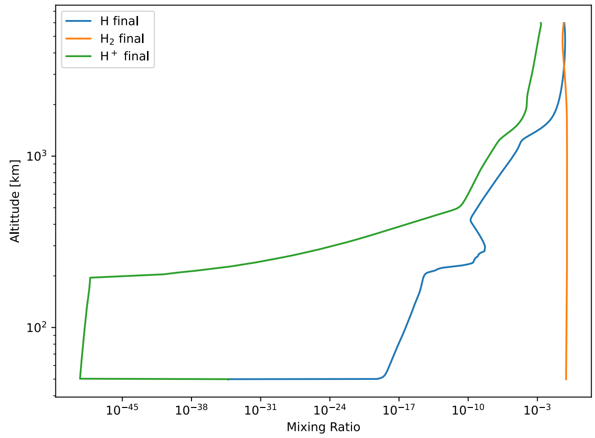

Figure 5.6: Species profiles of case with, $\log(X_{H_2}) = -0.82$ and the exobase limited to 6,000 km. In the upper atmosphere H and H_2 are nearly equally abundant, due to exposure to high energetic radiation. This distribution starts to change quite drastically below $\sim 2 \cdot 10^3$ km.

$\log(X_{H_2O})$	$\log(X_H)$	$\log(X_{H_2})$	$\log(X_{H^+})$	$\log(X_{total})$
$-0.82^\star$	-0.2945	-0.3119	-2.6234	-0.0011
-1.30	N/A	N/A	N/A	N/A
$-1.70^\star$	-0.3325	-0.2756	-2.6038	-0.0010
$-2.00^\star$	-0.2849	-0.3223	-2.6126	-0.0011
$-2.30^\star$	-0.2871	-0.3200	-2.5918	-0.0011
$-2.70^\star$	-0.2880	-0.3189	-2.5969	-0.0011
$-3.70^\star$	-0.2865	-0.3207	-2.5918	-0.0011

Table 5.4: Three most dominant species at the exobase of 7,000 km for multiple water content scenarios at the end of a stable simulation. These three species make up at least 99.7 % of the volume mixing ratio. Therefore, the other species are considered irrelevant to the overall process as they also have small loss rates. Simulations marked with * are post-processed because they showed a small evolution even though the code claimed that they were stable. The run with $\log(X_{H_2O}) = -1.30$ unfortunately did not finish in time.

above. Three different atmospheric masses have been included in this consideration, because there are three scenarios proposed by Madhusudhan et al. 2020, all of which fit the data equally well in terms of overall planetary density and atmospheric composition. It is important to note that a mass loss of one atmospheric mass does not mean there is no atmosphere left since effects such as outgasing cannot be taken into account.

$\log(X_{H_2O})$	H loss rate [g s-1]	H_2 loss rate [g s-1]	H^+ loss rate [g s-1]
$-0.82^\star$	$0.613 \cdot 10^8$	$0.295 \cdot 10^5$	$0.259 \cdot 10^6$
-1.30	N/A	N/A	N/A
$-1.70^\star$	$0.491 \cdot 10^8$	$0.227 \cdot 10^5$	$0.231 \cdot 10^6$
$-2.00^\star$	$0.542 \cdot 10^8$	$0.265 \cdot 10^5$	$0.245 \cdot 10^6$
$-2.30^\star$	$0.498 \cdot 10^8$	$0.265 \cdot 10^5$	$0.0238 \cdot 10^6$
$-2.70^\star$	$0.516 \cdot 10^8$	$0.270 \cdot 10^5$	$0.0242 \cdot 10^6$
$-3.70^\star$	$0.494 \cdot 10^8$	$0.263 \cdot 10^5$	$0.238 \cdot 10^6$

Table 5.5: Loss rates of the three most dominant species for multiple water contents with the exobase limited to 6,000 km. The loss rates of the other species are at least six orders of magnitude lower than the lowest value listed and are therefore considered irrelevant to the overall process. Simulations marked with * are post-processed as they showed a small evolution, although the code deemed them to be stable. The run with $\log(X_{H_2O}) = -1.30$ unfortunately did not finish in time.

$\log(X_{H_2O})$	H loss rate [g s-1]	H_2 loss rate [g s-1]	H^+ loss rate [g s-1]
$-0.82^\star$	$0.620 \cdot 10^8$	$0.634 \cdot 10^5$	$0.303 \cdot 10^6$
-1.30	N/A	N/A	N/A
$-1.70^\star$	$0.527 \cdot 10^8$	$0.504 \cdot 10^5$	$0.282 \cdot 10^6$
$-2.00^\star$	$0.572 \cdot 10^8$	$0.561 \cdot 10^5$	$0.293 \cdot 10^6$
$-2.30^\star$	$0.539 \cdot 10^8$	$0.568 \cdot 10^5$	$0.288 \cdot 10^6$
$-2.70^\star$	$0.551 \cdot 10^8$	0.57710^5	$0.290 \cdot 10^6$
$-3.70^\star$	$0.536 \cdot 10^8$	$0.565 \cdot 10^5$	$0.287 \cdot 10^6$

Table 5.6: Loss rates of the three most dominant species for multiple water contents with the exobase limited to 7,000 km. The loss rates of the other species are at least six orders of magnitude lower than the lowest value listed and are therefore considered irrelevant to the overall process. Simulations marked with * are post-processed as they showed a small evolution, although the code deemed them to be stable. The run with $\log(X_{H_2O}) = -1.30$ unfortunately did not finish in time.

5.3 Atmospheric Lifetimes

In Figure 5.7 the lifetimes of Table 5.7 and Table 5.8 are visualized for an easier discussion. The figure shows the results of a total of 12 simulations, which result in 36 different possible outcomes for K2-18 b as there are three proposed scenarios by Madhusudhan et al. 2020. The different lifetimes scatter significantly and correlate to the three scenarios. The cases for the scenario with an atmospheric mass fraction of 5 % were cropped out of the image and accounted for by red upwards pointing triangles as the lifetimes are much longer at around 4,000 Gyr. There are also two horizontal lines added, the dotted one at 14 Gyr

$\log(X_{2O)}$	total loss rate $[gs^{-1}]$	$t^{5.0\%}_{\text{vanish}}[Gyr]$	$t^{0.03\%}_{\text{vanish}}[Gyr]$	$t^{0.006\%}_{\text{vanish}}[Gyr]$
$-0.82^{\star}$	$0.323 \cdot 10^8$	3505	15.15	3.03
-1.30	N/A	N/A	N/A	N/A
$-1.70^{\star}$	$0.245 \cdot 10^8$	4630	20.02	4.01
$-2.00^{\star}$	$0.280 \cdot 10^8$	4054	17.53	3.51
$-2.30^{\star}$	$0.256 \cdot 10^8$	4428	19.14	3.83
$-2.70^{\star}$	$0.267 \cdot 10^8$	4423	18.39	3.68
$-3.70^{\star}$	$0.254 \cdot 10^8$	4470	19.33	3.87

Table 5.7: The total mass loss rate due to H, H^2, and H^+, and the resulting lifetime of the atmosphere, i.e., the time it would take for the mass of the atmosphere to disappear once, for the three scenarios Madhusudhan et al. 2020 proposed, all of which fit the data equally well if evolution is not taken into account. These cases are for the exobase limitation at 6,000 km. The run with $\log(X_{\text{H}_2\text{O}}) = -1.30$ unfortunately did not finish in time.

$\log(X_{\text{H}_2\text{O}})$	total loss rate $[gs^{-1}]$	$t^{5.0\%}_{\text{vanish}}[Gyr]$	$t^{0.03\%}_{\text{vanish}}[Gyr]$	$t^{0.006\%}_{\text{vanish}}[Gyr]$
$-0.82^{\star}$	$0.315 \cdot 10^8$	3599	15.56	3.12
-1.30	N/A	N/A	N/A	N/A
$-1.70^{\star}$	$0.245 \cdot 10^8$	4622	19.98	4.00
$-2.00^{\star}$	$0.297 \cdot 10^8$	3816	16.50	3.30
$-2.30^{\star}$	$0.279 \cdot 10^8$	4070	17.60	3.52
$-2.70^{\star}$	$0.284 \cdot 10^8$	3990	17.25	3.45
$-3.70^{\star}$	$0.277 \cdot 10^8$	4087	17.67	3.54

Table 5.8: The total mass loss rate due to H, H^2, and H^+, and the resulting lifetime of the atmosphere, i.e., the time it would take for the mass of the atmosphere to disappear once, for the three scenarios Madhusudhan et al. 2020 proposed, all of which fit the data equally well if evolution is not taken into account. These cases are for the exobase limitation at 7,000 km. The run with $\log(X_{\text{H}_2\text{O}}) = -1.30$ unfortunately did not finish in time.

marking the lifetime of the universe and a dashed one marking the current accepted age of 4.0 Gyr of K2-18. The dashed line is surrounded by a grey shaded area representing the 1 σ of the age as determined by Gaidos et al. 2023. The squares mark the lifetimes [3] if the exobase is limited to 6,000 km and the circles show the case of the limit being set at 7,000 km. The colours represent the scenarios by Madhusudhan et al. 2020 (see Figure 2 of the paper and chapter chapter 3 of this thesis). The two exobase limitations for each scenario and water content are connected with a black vertical line as the exobase limitations were

[3]Lifetime here reffers to the atmospheric lifetime, i.e. the time needed that the entire mass of the atmosphere is lost one time. This lifetime does not account for any other effects that my affect the atmospheric mass like outgasing, impact events, etc..

chosen arbitrarily. Overall, it can be seen that the water content does not play a big role for the development of the atmosphere. Instead, the existence of water itself is the relevant factor for its lifetime. Comparing these results to the first case presented here, which was simulated with no water at all and would also lie out of the plotted area as even the predicted lifetime for the least massive atmospheric scenario is already nearly 80 Gyr. Nonetheless, a minor trend showing that higher amounts of water resulting in slightly lower lifetimes is visible. More striking is the fact that for the cases with a small amount of water the 7,000 km exobase limitation led to elongated lifetimes whereas for higher amounts of water this starts to flip and the limit at 6,000 km supports slightly longer lifetimes.

For the discussion I will group the lifetime into three larger groups, the first group consisting of lifetimes which are larger than 14 Gyr, the second one of lifetimes which are below 14 Gyr but above 6.34 Gyr, and the last one of lifetimes which are within the uncertainties of the age of K2-18, i.e. 4.0 ± 2.34 Gyr (Gaidos et al. 2023).

5.3.1 Atmospheric Lifetime Larger Than 14 Gyr

There are 24 cases for which my simulations predict a lifetime over 14 Gyr. These cases are all from the scenarios for which Madhusudhan et al. 2020 proposed an atmospheric mass fraction of 5 % and 0.03 %.

Looking at actual numbers it quickly becomes clear that all cases for a 5 % mass fraction atmosphere are stable long-term. Lifetimes exceeding 4000 Gyr are beyond human comprehension. Any prediction of such an excessive timescale would be highly theoretical and would not lead to any reliable conclusion. Therefore, the most massive predicted atmosphere with a mass fraction of 5 % should definitely be considered stable. This does not mean K2-18b has no primary or secondary atmosphere as all the cases between $\log(X_{H_2O})$ = -0.82 and -3.70 predict such elongated lifetimes. Regarding habitability as we define it in chapter 1 , it can be said, that K2-18b neither is nor will become habitable in the sense earth is.

The scenarios which predict lifetimes below 20 Gyr for the atmosphere with a mass fraction of 0.03 % need to be considered separately. These scenarios are still stable on the time scales for known lifeforms, but on astronomical scales this comes in relatable ranges. Taking into account that the system is already 4 Gyr old leads to the conclusion that an atmosphere with a mass fraction of 0.03 % might get lost within the next 10 to 15 Gyr. These scenarios, therefore, are currently not habitable as we understand it, but they might be sometime in the future. It should be mentioned again that an atmospheric mass loss in an order of magnitude of the atmospheric mass does not necessarily indicate that there is no more atmosphere at all – this would also be hostile to life – but that the atmosphere has undergone drastic changes in its size and composition. Any atmosphere that may arise would have to be outgased from the planet and therefore, be rich in heavier species such as oxygen, nitrogen or ammonia, to name a few possibilities.

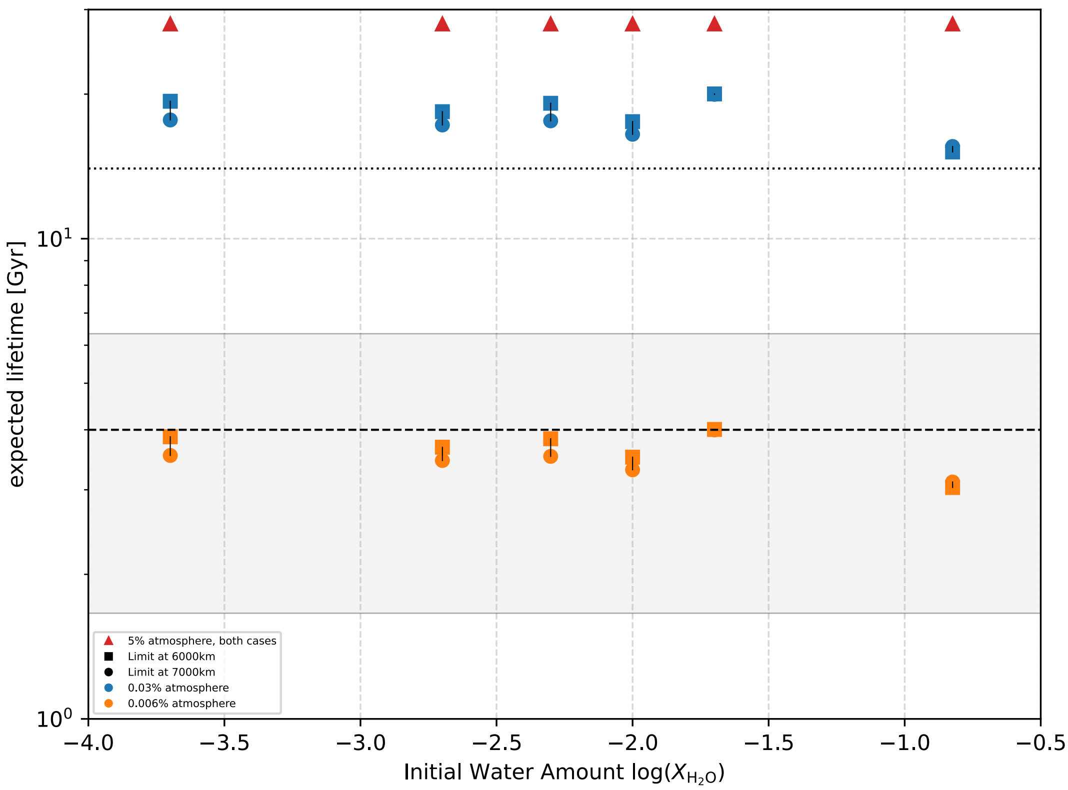

Figure 5.7: Lifetimes of different atmospheric mass scenarios proposed by Madhusudhan et al. 2020 with different amounts of water in the atmosphere. The horizontal lines mark 14 Gyr and 4 Gyr, i.e. lifetime of the universe resp. the stellar system. The grey band represents the uncertainty of the age of the stellar system.

5.3.2 Atmospheric Lifetime Between 6.34 Gyr and 14 Gyr

None of my simulations predicted lifetimes in this range . I will nevertheless discuss such an atmosphere as there are some arbitrary factors which could shift my simulations in this region.

The most dominant factor in this case is the exobase limitation. As aforementioned, the sign of the difference between the 6,000 km case and 7,000 km one depends on the water content. Therefore, depending on the water content increasing or decreasing the exobase limitation may shift and place the lifetime into a range above 6.34 Gyr. It might be possible for the case $\log(X_{H_2O}) = -0.82$ and an atmospheric mass fraction of 0.006 %

to be shifted from below 4.0 Gyr upwards or for the low amounts and a 0.03 % mass fraction downwards below 14 Gyr.

These cases would then have a remaining lifetime between $\sim$ 10 Gyr and $\sim$ 2.5 Gyr, taking into account that the system is 4.0 Gyr old. As we know from multiple dwarf stars which already exceeded the lifetime of 10 Gyr (e.g., Gaidos et al. 2023) it can be rather safely assumed that K2-18 will stay long enough on the main sequence to provide a stable amount of radiation for a long enough time to strip K2-18b's atmosphere. Therefore, it could make space for a non-hydrogen dominated atmosphere which in turn would allow for more complex chemical processes, which are considered beneficial for the arising of simple lifeforms.

5.3.3 Atmospheric Lifetime Below 6.34 Gyr

Now to the most conclusive cases and scenarios. My simulations predict multiple cases with an atmospheric lifetime between 1.66 Gyr and 6.34 Gyr, this is the 1 σ range around the best estimated lifetime of 4 Gyr by Gaidos et al. 2023. All the cases are part of the scenario with an atmospheric mass fraction of 0.006 %, the least massive scenario from the predictions by Madhusudhan et al. 2020. For this predicted lifetime multiple explanations are possible, all of which are equally probable.

The first possible interpretation I want to describe assumes that the lifetime of the atmosphere is indeed 4.0 Gyr or larger within 1 σ. This would mean that all the water abundance cases for the 0.006 % atmospheric mass fraction predict an atmospheric lifetime shorter than the age of the stellar system. Additionally, taking into account that younger stars are more active, this would lead to the conclusion that the atmosphere is already lost. As the atmosphere can still be observed this cannot be true. In consequence, this indicates that atmospheres with such a low mass are not a possible scenario for K2-18b. The other equally feasible interpretation assumes that the least massive scenario for the atmosphere of Madhusudhan et al. 2020 with an atmospheric mass fraction of 0.006 % is an option and we can observe it. As my simulations predict atmospheric lifetimes between 2 Gyr and 4 Gyr this would lead to the constraint that K2-18 is not as old as assumed by Gaidos et al. 2023 or at least close to the lowest possible prediction within 1 σ. Here, it is also necessary to discuss the arbitrary placement of the exobase limitations. Especially the cases with low water mixing ratios and the exobase limited to 6,000 km predict lifetimes close to 4.0 Gyr . If the limitation is set to 5,000 km, the predicted atmospheric lifetime would most properly be longer than 4.0 Gyr and a feasible scenario. For a currently unknown reason this trend flips towards the high water abundance . For $\log(X_{\mathrm{H_2O}}) = -0.82$, therefore, a higher exobase limitation would lead to a longer atmospheric lifetime, which might become larger than 4.0 Gyr. Conclusively, it is not possible to put unambiguous constrains on the atmospheric nature of K2-18 b by simulations only. Further observational constraints either on the atmospheric compositions or on the stellar age are necessary to do this.

5.4 Pressure Profiles

Besides studying the loss rates and lifetimes of the simulated cases I also looked into the pressure-temperature profiles of the different cases. I will discuss the $\log(X_{H_2O}) = -0.82$ case limited to 6,000 km exemplary as it shows the features I want to discuss the best , but overall they all are very similar. The remaining plots are shown in the appendix A.1.

The pressure-temperature profile is shown in Figure 5.8. On the x axis the temperature in Kelvin is shown, it reaches from $\sim$ 255 K – the equilibrium temperature as determined by Benneke et al. 2019 – up to $\sim$ 2250 K. There are two y axes, one depicting the pressure and one the according simulation altitude. The pressure range starts at $\sim 10^{-1}$ bar at a simulation altitude of $\sim$ 100 km and goes down to 10^9 bar at $5 \cdot 10^3$ km simulation height. The exact altitude above the surface is hard to distinguish as it highly depends on the nature of the planetary core , which is quite ambiguous as can be seen by comparing the scenarios of Madhusudhan et al. 2020. It is necessary to mention at this point that the well-studied and originally planned pressure regime of the Kompot code does not reach up to 10^{-1} bar, but stops at 10^{-3} bar. Therefore, one must be cautious reading too much into these *high pressure* regimes.

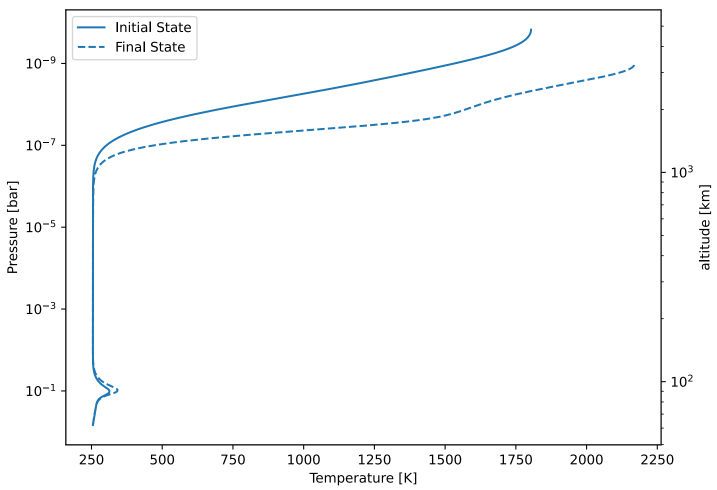

Figure 5.8: Pressure-Temperature profile of the case with $\log(X_{H_2}) = -0.82$ and the exobase limited to 6,000 km. It can be split in an isothermal part in the center between 10^{-1} bar and 10^{-7} bar, a small bump at $\sim 10^{-1}$ bar, and a part were the atmosphere is actually heated up below 10^{-7} bar in the top part.

The profile can be split into three prominent features: the main part of the profile between 10^{-7} bar and 10^{-1} bar is isothermal and does not change during the simulations. At (or slightly below in other cases) 10^{-1} bar is a small bump in the profile, and starting at $\sim 10^{-7}$ bar the atmosphere heats up a lot. This is due to the absorption of EUV radiation in the upper layers of the atmosphere. EUV radiation is important to the heating mechanism presented in (chapter chapter 2) and only $\sim$ 11.5 % of the EUV flux reaches down to 1,000km to heat up the lower layers of the atmosphere.

This also explains the difference between the profile at the beginning of the simulation[4] and the final state. It clearly indicates that the main heat source for the upper atmosphere is indeed the EUV irradiation of K2-18. For comparison only, $\sim$ 40 % of the X-Rays flux has been absorbed at the altitude of 1,000 km. In Figure 5.9 the two absorption profiles are shown for $\log(X_{H_2O}) = -0.82$ and the exobase limitation set to 6,000 km. The rest can be found in the appendix A.1. If the main energy source for the heating would be something different , e.g., X-Rays, we would expect a much smaller or larger isothermal part in the profile. The small bump at $\sim 10^{-1}$ bar is most probably due to reactions including the creation and destruction of H_2O and subsequent O_2, which can cause a lot of heat (Johnstone et al. 2018).

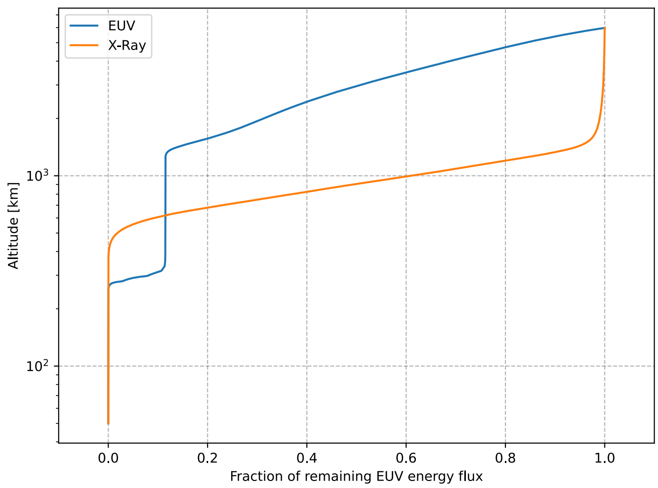

Figure 5.9: Absorption profiles of EUV and X-Rays depending on way through the atmosphere. EUV is mainly absorbed above 10^3 km, whereas X-Rays are mostly absorbed between $1.5 \cdot 10^3$ km and $5 \cdot 10^2$ km.

The other profile is an altitude-pressure profile. Here, only the case for $\log(X_{H_2O}) = -0.82$ at 6,000 km is shown in Figure 5.9, the rest can be found in the appendix A.1. This profile shows that the main evolution of the atmosphere happens in the upper atmosphere above $\sim 10^3$ km (respectively below a pressure of $\sim 10^{-7}$ bar). This emphasizes the major influence of the host star's irradiation received by the planet on the nature of the

[4]Beginning in this case means the restart of the simulation at 0.159 AU after the temperatures were merged.

planet and therefore, its potential habitability.

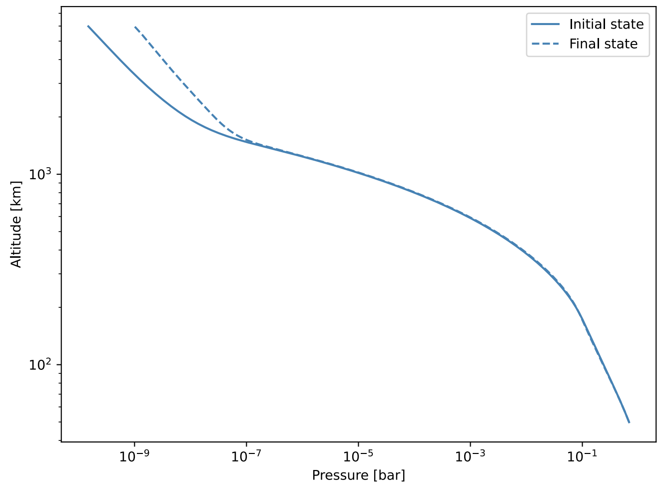

Figure 5.10: Altitude-pressure profile of the case with $\log(X_{\mathrm{H_2}}) = -0.82$ and the exobase limited to 6,000 km. It can be seen that the large difference between the beginning and the end of the simulation only affects the region above $\sim$ 1,000 km and below $\sim 10^{-7}$ bar.

5.5 Determining the Simulation Speed

To have a measurand for the accuracy of the simulations I chose to compare the Jeans mass loss rate of atomic hydrogen with one another. Speed – the other relevant factor – was determined by dividing the elapsed domain time to stabilization by the runtime up to that point. Table 5.9 lists the bin number, the initial water content, the Jeans mass loss rate of atomic hydrogen at stabilization, the stabilization time for the domain and the real world, and the speed of the simulations, i.e., how many days are simulated within one day. Comparing the stabilization time of the domain and the Jeans mass loss rate of atomic hydrogen, the number of bins does not seem to have a large effect. Still, it should be noted that the mass loss rate for 100 and 10 bins is lower than for all other scenarios for each initial water content. Since a higher resolution of the spectrum in the XUV regime leads to a more accurate simulation, it should be assumed that going below 250 XUV bins worsens the results of the simulations, while there is no difference between 250 and 1000 bins. The stabilization domain time is still identical in each case.

Looking at the simulation speed we can see that 100 bins work best for each initial water content. But comparing the speed with 1000 bins, at least for 1.0 % water, it does not make a substantial difference, which is tolerable considering the more accurate simulation. It can be concluded that the chemical composition and, therefore, the chemical network of the computational code has a bigger impact on the simulation speed than the XUV binning. A possible explanation for the inferior performance in terms of speed and accuracy of 10 bins is that this coarse binning leads to extensive heating in the cells, which triggers many chemical reactions, which in turn take time to calculate.

XUV_{bins}	H_2O_{init}[%]	Jeans rate $_{\mathrm{H}}$ $[g\ s^{-1}]$	t^{stab}_{dom} [d]	t^{stab}_{real} [d]	*Speed* $[\mathrm{d_{dom}/d_{real}}]$
1000	1.0	$0.254 \cdot 10^{-9}$	6.39	2.49	2.57
750	1.0	$0.254 \cdot 10^{-9}$	6.39	3.01	2.12
500	1.0	$0.254 \cdot 10^{-9}$	6.39	3.34	1.91
250	1.0	$0.254 \cdot 10^{-9}$	6.39	3.29	1.94
100	1.0	$0.243 \cdot 10^{-9}$	6.39	2.43	2.63
10	1.0	N/A	N/A	N/A	N/A
1000	0.5	N/A	N/A	N/A	N/A
750	0.5	$0.209 \cdot 10^{-9}$	6.31	2.69	2.35
500	0.5	$0.209 \cdot 10^{-9}$	6.31	2.66	2.37
250	0.5	$0.210 \cdot 10^{-9}$	6.31	2.77	2.28
100	0.5	$0.201 \cdot 10^{-9}$	6.31	1.98	3.19
10	0.5	$0.110 \cdot 10^{-9}$	6.31	4.77	1.58

Table 5.9: Mass loss rate, stabilization time and *speed* of the simulations for twelve different scenarios. Varying the initial water content and the number of XUV bins used. The scenarios with 10 bins and 1.0% initial water content and 1000 bins and 0.5% initial water content crashed before the Kompot coded flagged a stable solution. It can be seen that the simulations with 100 bins are the fastest option but achieve lower Jeans mass loss rates than the scenarios with more bins. For the 1% water scenarios, the 1,000 bins simulation is not much slower.

6 Conclusion and Outlook

Conclusion

In this thesis I looked at the atmospheric composition and short-term evolution of K2-18 b as well as at different possible mass loss scenarios for the atmosphere. I simulated a wide variety of atmospheres using the Kompot code with the focus on different water abundances within the observational constraints determined infrared and optical observationbs Benneke et al. 2019, Tsiaras et al. 2019, and Madhusudhan et al. 2020.

All simulations were done iteratively, where the planet first was at 1 AU orbital distance and then reduced step by step to reach K2-18 b's actual orbital distance at 0.159 AU. This was done to avoid numerical instabilities, due to too many chemical reactions as a result of the steep increase in temperature. All cases were started with separated temperatures, which turned out not to be necessary for all cases as the temperature for the neutrals, ions, and electrons, were identical in the end. Some cases were post-processed, which means that the separated – but identical – temperatures were merged and the simulation were restarted with different exobase limitations. Due to its light weight, the hydrogen dominated atmosphere immediately expanded to this new limitation. However, the overall results in terms of mass loss rates are almost identical.

My simulations show that of the three different scenarios proposed by Madhusudhan et al. 2020 the most massive one with an atmospheric mass fraction of 5 % is stable. Neither the arbitrary exobase limitation nor the initial amount of water have a relevant impact as the predicted lifetimes are all around 4000 Gyr, which is beyond our comprehension, even on cosmological timescales.

On the other hand, the atmospheres with 0.03 % of the total planetary mass have a much lower lifetime between 14 and 20 Gyr. Even though this still a long time for any lifeform, it is on a more relatable timescales of the universe on which stellar processes become better understood. Therefore, such an atmosphere might get lost and replaced by an outgased one, which could be more compact and richer in heavier species and hence, will not vanish as fast.

The third and least massive scenario as proposed by Madhusudhan et al. 2020 had an atmospheric mass of 0.006 % of the total mass of K2-18 b. All the simulated cases would get lost in less than 4.0 Gyr. This either indicates that the system must be younger than 4.0 Gyr, which would be possible as all the predicted lifetimes are within 1 for the lifetime of K2-18 as proposed by Gaidos et al. 2023. Otherwise it could rule out that K2-18 b has an atmosphere this low in mass. Including stellar activity evolution and onsidering that younger stars are more active and have higher XUV fluxes, which lead to significant higher mass loss rates in earlier times (Güdel 2007). Combining this knowledge on stellar evolution and my simulations leads to the conclusion that the least massive atmospheric mass fraction scenario is disfavoured.

As the behavior of the different cases is not very dependent on the water content my simulations unfortunately cannot constrain it. But this is also currently not possible by observational data as shown in Figure 6.1. It shows eight theoretical transit spectra of K2-18 b, which I simulated, with different water contents from the lowest 0.002 % to the hypothetical 50 % of Tsiaras et al. 2019. The difference between these two scenarios peeks between 1 μm and 3 μm and reaches up to ∼ 30 ppm. Looking back to Figure 3.1 of Benneke et al. 2019 it becomes clear why the uncertainty in the water content is so high, as even the smallest error bars cover ∼ 50 ppm.

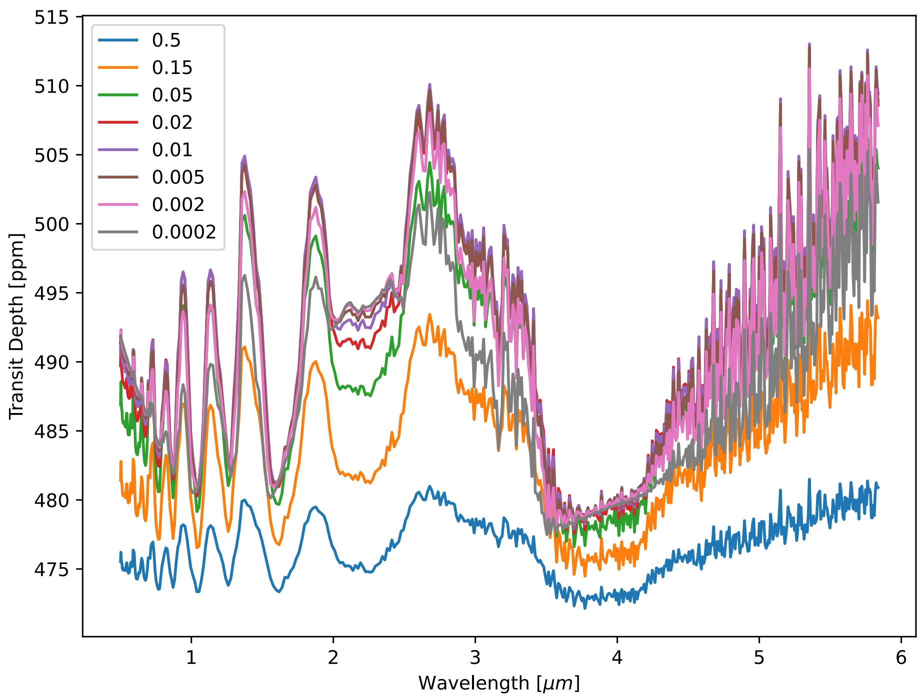

Figure 6.1: Theoretical transit spectra for hydrogen dominated atmospheres with different water contents of K2-18 b depending on the water content. The difference between the least abundant case (0.002 %) and the hypothetical most abundant case of Tsiaras et al. 2019 (50 %) is rougly 30 ppm. Simulations provided by Simon Schleich, a PhD student at University of Vienna.

Future Outlook

Combining the similar evolutionary behavior and the small spectral impact of different water contents it is clear that it will not be possible to constrain the water content any further without further observational data either by JWST. An important limitation which has to be mentioned is that the existence of CH_4 had to be neglected in this thesis as it is not yet included in the Kompot code. Methane would introduce carbon as a new element to the atmospheric mixture, this carbin than can form CO_2 and CO if combined with oxygen from the water. Even though carbon dioxide acts as a greenhouse gas in the lower atmosphere, it is a major coolant in the upper parts. Considering that the mass loss is mainly driven by the temperature of the top layer of the atmosphere, already a small cool down can have a huge impact on the loss rate and therefore the lifetime of the atmosphere.

Due to the uncertainty of how much water and methane is actually in the atmosphere, further observations of other wavelengths by JWST and Ariel are important as they will have a significant impact on this understanding. This will increase the accuracy of simulations like mine, which are the only way to determine, if the different scenarios proposed based on observational data of an atmosphere that is stable enough so that we can actually observe them. Of course, these theoretical studies on the lifetime of planetary atmosphere do not cover every detail of the atmospheric loss processes, but in general they help to outline some expectations for potential evolutionary pathways for K2-18 b.

Bibliography

Allard, F., D. Homeier and B. Freytag (June 2012). “Models of very-low-mass stars, brown dwarfs and exoplanets”. In: *Philosophical Transactions of the Royal Society of London Series A* 370.1968, pp. 2765–2777. DOI: 10.1098/rsta.2011.0269. arXiv: 1112.3591 [astro-ph.SR].

Anglada-Escudé, Guillem et al. (Aug. 2016). “A terrestrial planet candidate in a temperate orbit around Proxima Centauri”. In: 536.7617, pp. 437–440. DOI: 10.1038/nature19106. arXiv: 1609.03449 [astro-ph.EP].

Armitage, Philip J (2020). *Astrophysics of Planet Formation.* eng. Cambridge: Cambridge University Press. ISBN: 9781108420501.

Banks, P. M. and G. Kockarts (1973). *Aeronomy.*

Barclay, Thomas et al. (Dec. 2021). “Stellar Surface Inhomogeneities as a Potential Source of the Atmospheric Signal Detected in the K2-18b Transmission Spectrum”. In: 162.6, 300, p. 300. DOI: 10.3847/1538-3881/ac2824. arXiv: 2109.14608 [astro-ph.EP].

Bean, Jacob L., Sean N. Raymond and James E. Owen (Jan. 2021). “The Nature and Origins of Sub-Neptune Size Planets”. In: *Journal of Geophysical Research (Planets)* 126.1, e06639, e06639. DOI: 10.1029/2020JE006639. arXiv: 2010.11867 [astro-ph.EP].

Benneke, Björn and Sara Seager (Dec. 2013). “How to Distinguish between Cloudy Mini-Neptunes and Water/Volatile-dominated Super-Earths”. In: 778.2, 153, p. 153. DOI: 10.1088/0004-637X/778/2/153. arXiv: 1306.6325 [astro-ph.EP].

Benneke, Björn et al. (Jan. 2017). “Spitzer Observations Confirm and Rescue the Habitable-zone Super-Earth K2-18b for Future Characterization”. In: 834.2, 187, p. 187. DOI: 10.3847/1538-4357/834/2/187. arXiv: 1610.07249 [astro-ph.EP].

Benneke, Björn et al. (Dec. 2019). “Water Vapor and Clouds on the Habitable-zone Sub-Neptune Exoplanet K2-18b”. In: 887.1, L14, p. L14. DOI: 10.3847/2041-8213/ab59dc. arXiv: 1909.04642 [astro-ph.EP].

Bézard, Bruno, Benjamin Charnay and Doriann Blain (Nov. 2020). “Methane as a dominant absorber in the habitable-zone sub-Neptune K2-18 b”. In: *arXiv e-prints*, arXiv:2011.10424, arXiv:2011.10424. DOI: 10.48550/arXiv.2011.10424. arXiv: 2011.10424 [astro-ph.EP].

Bouvier, J. et al. (Jan. 2014). “Angular Momentum Evolution of Young Low-Mass Stars and Brown Dwarfs: Observations and Theory”. In: *Protostars and Planets VI.* Ed. by Henrik Beuther et al., pp. 433–450. DOI: 10.2458/azu_uapress_9780816531240-ch019. arXiv: 1309.7851 [astro-ph.SR].

Carroll, Bradley W. (2017). *An introduction to modern astrophysics.* eng. Second edition. Cambridge : Cambridge University Press, ISBN: 9781108380980.

Catling, David (David Charles) (2017). *Atmospheric evolution on inhabited and lifeless worlds.* eng. Cambridge : Cambridge University Press. ISBN: 1-316-82380-6.

Charnay, B. et al. (Feb. 2021). “Formation and dynamics of water clouds on temperate sub-Neptunes: the example of K2-18b”. In: 646, A171, A171. DOI: `10.1051/0004-6361/202039525`. arXiv: `2011.11553 [astro-ph.EP]`.

Charnay, Benjamin et al. (Sept. 2020). “Formation and dynamics of water clouds on K2-18 b”. In: *European Planetary Science Congress*, EPSC2020-889, EPSC2020–889. DOI: `10.5194/epsc2020-889`.

Chaufray, J. Y. (Apr. 2021). “Departure of the thermal escape rate from the jeans escape rate for atomic hydrogen at Earth, Mars, and Pluto”. In: 198, 105178, p. 105178. DOI: `10.1016/j.pss.2021.105178`.

Christie, Duncan A. et al. (Nov. 2022). “CAMEMBERT: A Mini-Neptunes General Circulation Model Intercomparison, Protocol Version 1.0.A CUISINES Model Intercomparison Project”. In: 3.11, 261, p. 261. DOI: `10.3847/PSJ/ac9dfe`. arXiv: `2211.04048 [astro-ph.EP]`.

Cloutier, R. et al. (Jan. 2019). “Confirmation of the radial velocity super-Earth K2-18c with HARPS and CARMENES”. In: 621, A49, A49. DOI: `10.1051/0004-6361/201833995`. arXiv: `1810.04731 [astro-ph.EP]`.

CRC handbook of chemistry and physics : a ready-reference book of chemical and physical data (1977). eng. Boca Raton, Fla. [u.a.]: Chemical Rubber Company VerfasserIn.

Dickinson, R. E. (Nov. 1972). “Infrared radiative heating and cooling in the Venusian mesosphere. I. Global mean radiative equilibrium.” In: *Journal of Atmospheric Sciences* 29, pp. 1531–1556. DOI: 10.1175/1520-0469(1972)029<1531:IRHACI>2.0.CO;2.

Dressel, Linda and Mariarosa Marinelli (2023). “WFC3 Instrument Handbook for Cycle 31 v. 15.0”. In: *WFC3 Instrument Handbook for Cycle 31 v. 15.0*. Vol. 15, p. 15.

France, Kevin et al. (Apr. 2016). “The MUSCLES Treasury Survey. I. Motivation and Overview”. In: 820.2, 89, p. 89. DOI: `10.3847/0004-637X/820/2/89`. arXiv: `1602.09142 [astro-ph.SR]`.

Fulton, Benjamin J. et al. (Sept. 2017). “The California-Kepler Survey. III. A Gap in the Radius Distribution of Small Planets”. In: 154.3, 109, p. 109. DOI: `10.3847/1538-3881/aa80eb`. arXiv: `1703.10375 [astro-ph.EP]`.

Gaidos, E. (Sept. 2017). “A minimum mass nebula for M dwarfs”. In: 470.1, pp. L1–L5. DOI: `10.1093/mnrasl/slx063`. arXiv: `1704.03265 [astro-ph.EP]`.

Gaidos, Eric et al. (Apr. 2023). “The TIME Table: rotation and ages of cool exoplanet host stars”. In: 520.4, pp. 5283–5304. DOI: `10.1093/mnras/stad343`. arXiv: `2301.12109 [astro-ph.EP]`.

Güdel, Manuel (Dec. 2007). “The Sun in Time: Activity and Environment”. In: *Living Reviews in Solar Physics* 4.1, 3, p. 3. DOI: `10.12942/lrsp-2007-3`. arXiv: `0712.1763 [astro-ph]`.

Hu, Renyu and Mario Damiano (Mar. 2021). *Deep Characterization of the Atmosphere of a Temperate Sub-Neptune*. JWST Proposal. Cycle 1, ID. #2372.

Johnstone, C. P. et al. (Sept. 2018). “Upper atmospheres of terrestrial planets: Carbon dioxide cooling and the Earth’s thermospheric evolution”. In: 617, A107, A107. DOI: `10.1051/0004-6361/201832776`. arXiv: `1806.06897 [astro-ph.EP]`.

Johnstone, Colin P. (Oct. 2017). "The Influences of Stellar Activity on Planetary Atmospheres". In: *Living Around Active Stars*. Ed. by D. Nandy, A. Valio and P. Petit. Vol. 328, pp. 168–179. DOI: 10.1017/S1743921317003775.

Kasting, James F., Daniel P. Whitmire and Ray T. Reynolds (Jan. 1993). "Habitable Zones around Main Sequence Stars". In: 101.1, pp. 108–128. DOI: 10.1006/icar.1993.1010.

Kopparapu, Ravi Kumar et al. (Mar. 2013). "Habitable Zones around Main-sequence Stars: New Estimates". In: 765.2, 131, p. 131. DOI: 10.1088/0004-637X/765/2/131. arXiv: 1301.6674 [astro-ph.EP].

Lissauer, Jack J and Imke de Pater (2013). *Fundamental Planetary Science: Physics, Chemistry and Habitability*. eng. New York: Cambridge University Press. ISBN: 9780521853309.

Loyd, R. O. P. et al. (June 2016). "The MUSCLES Treasury Survey. III. X-Ray to Infrared Spectra of 11 M and K Stars Hosting Planets". In: 824.2, 102, p. 102. DOI: 10.3847/0004-637X/824/2/102. arXiv: 1604.04776 [astro-ph.SR].

Madhusudhan, Nikku et al. (Mar. 2020). "The Interior and Atmosphere of the Habitable-zone Exoplanet K2-18b". In: 891.1, L7, p. L7. DOI: 10.3847/2041-8213/ab7229. arXiv: 2002.11115 [astro-ph.EP].

Madhusudhan, Nikku et al. (Mar. 2021). *Chemical Disequilibrium in a Temperate sub-Neptune*. JWST Proposal. Cycle 1, ID. #2722.

Mayor, Michel and Didier Queloz (Nov. 1995). "A Jupiter-mass companion to a solar-type star". In: 378.6555, pp. 355–359. DOI: 10.1038/378355a0.

Meadows, Victoria S. (2008). "Planetary Environmental Signatures for Habitability and Life". In: *Exoplanets: Detection, Formation, Properties, Habitability*. Ed. by John W. Mason. Berlin, Heidelberg: Springer Berlin Heidelberg, pp. 259–284. ISBN: 978-3-540-74008-7. DOI: 10.1007/978-3-540-74008-7_10. URL: https://doi.org/10.1007/978-3-540-74008-7_10.

Mercer, Anthony and Dimitris Stamatellos (Jan. 2020). "Planet formation around M dwarfs via disc instability. Fragmentation conditions and protoplanet properties". In: 633, A116, A116. DOI: 10.1051/0004-6361/201936954. arXiv: 2001.10062 [astro-ph.SR].

Molyarova, Tamara et al. (Nov. 2017). "Gas Mass Tracers in Protoplanetary Disks: CO is Still the Best". In: 849.2, 130, p. 130. DOI: 10.3847/1538-4357/aa9227. arXiv: 1710.02993 [astro-ph.EP].

Montet, Benjamin T. et al. (Aug. 2015). "Stellar and Planetary Properties of K2 Campaign 1 Candidates and Validation of 17 Planets, Including a Planet Receiving Earth-like Insolation". In: 809.1, 25, p. 25. DOI: 10.1088/0004-637X/809/1/25. arXiv: 1503.07866 [astro-ph.EP].

Mulders, Gijs D. et al. (July 2015). "The Snow Line in Viscous Disks around Low-mass Stars: Implications for Water Delivery to Terrestrial Planets in the Habitable Zone". In: 807.1, 9, p. 9. DOI: 10.1088/0004-637X/807/1/9. arXiv: 1505.03516 [astro-ph.EP].

NASA Exoplanet Archive (2023). *Planetary Systems*. Version Version: 2023-03-30 09:18. DOI: 10.26133/NEA12. URL: https://catcopy.ipac.caltech.edu/dois/doi.php?id=10.26133/NEA12.

Rigby, Jane et al. (July 2022). "The Science Performance of JWST as Characterized in Commissioning". In: *arXiv e-prints*, arXiv:2207.05632, arXiv:2207.05632. DOI: 10.48550/arXiv.2207.05632. arXiv: 2207.05632 [astro-ph.IM].

Schweitzer, A. et al. (May 2019). "The CARMENES search for exoplanets around M dwarfs. Different roads to radii and masses of the target stars". In: 625, A68, A68. DOI: 10.1051/0004-6361/201834965. arXiv: 1904.03231 [astro-ph.SR].

Seager, Sara (2010). *Exoplanet atmospheres : physical processes*. eng. Princeton series in astrophysics. Princeton, NJ [u.a.]: Princeton Univ. Pr. ISBN: 9780691119144.

Sreejith, A. G. et al. (Dec. 2020). "Ca II H&K stellar activity parameter: a proxy for extreme ultraviolet stellar fluxes". In: 644, A67, A67. DOI: 10.1051/0004-6361/202039167. arXiv: 2010.16179 [astro-ph.SR].

Tinetti, Giovanni et al. (2020). *Ariel Definition Study Report (Red Book)*. URL: https://sci.esa.int/web/ariel/-/ariel-definition-study-report-red-book.

Tsiaras, Angelos et al. (Sept. 2019). "Water vapour in the atmosphere of the habitable-zone eight-Earth-mass planet K2-18 b". In: *Nature Astronomy* 3, pp. 1086–1091. DOI: 10.1038/s41550-019-0878-9. arXiv: 1909.05218 [astro-ph.EP].

von Braun, Kaspar et al. (Mar. 2014). "Stellar diameters and temperatures - V. 11 newly characterized exoplanet host stars". In: 438.3, pp. 2413–2425. DOI: 10.1093/mnras/stt2360. arXiv: 1312.1792 [astro-ph.EP].

West, Andrew A. et al. (Mar. 2008). "Constraining the Age-Activity Relation for Cool Stars: The Sloan Digital Sky Survey Data Release 5 Low-Mass Star Spectroscopic Sample". In: 135.3, pp. 785–795. DOI: 10.1088/0004-6256/135/3/785. arXiv: 0712.1590 [astro-ph].

Wordsworth, Robin and Laura Kreidberg (Aug. 2022). "Atmospheres of Rocky Exoplanets". In: 60, pp. 159–201. DOI: 10.1146/annurev-astro-052920-125632. arXiv: 2112.04663 [astro-ph.EP].

Wright, Nicholas J. et al. (2011). "THE STELLAR-ACTIVITY–ROTATION RELATIONSHIP AND THE EVOLUTION OF STELLAR DYNAMOS". In: *The Astrophysical Journal* 743.1, p. 48. DOI: 10.1088/0004-637X/743/1/48. URL: https://dx.doi.org/10.1088/0004-637X/743/1/48.

Youngblood, Allison et al. (June 2016). "The MUSCLES Treasury Survey. II. Intrinsic LYα and Extreme Ultraviolet Spectra of K and M Dwarfs with Exoplanets*". In: 824.2, 101, p. 101. DOI: 10.3847/0004-637X/824/2/101. arXiv: 1604.01032 [astro-ph.SR].

Appendix

A.1 Additional Figures

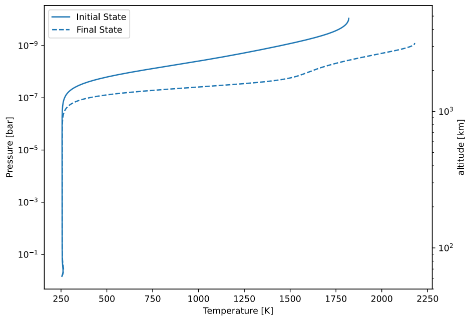

(a) $\log(X_{\mathrm{H_20}}) = -3.70$

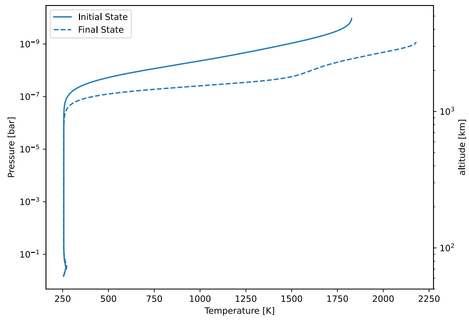

(b) $\log(X_{\mathrm{H_20}}) = -2.70$

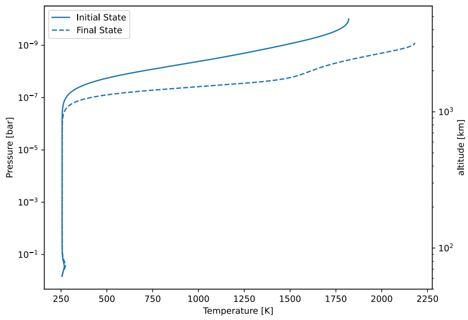

(c) $\log(X_{\mathrm{H_20}}) = -2.30$

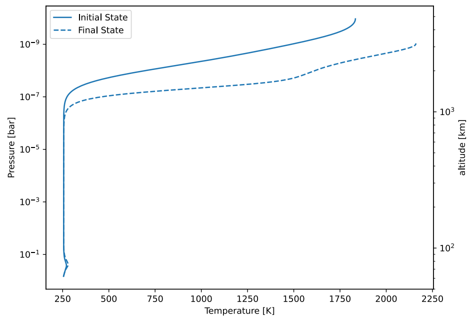

(d) $\log(X_{\mathrm{H_20}}) = -2.00$

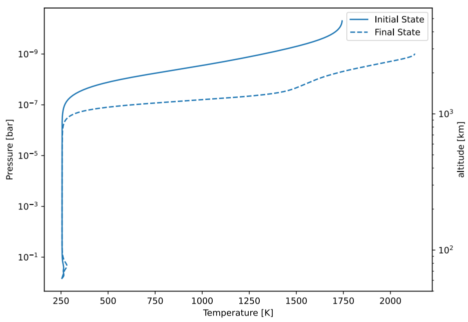

(e) $\log(X_{\mathrm{H_20}}) = -1.70$

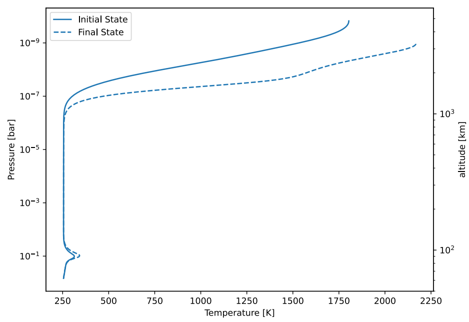

(f) $\log(X_{\mathrm{H_20}}) = -0.82$

Figure A.1: Pressure-temperature profiles for different water abundances, exobase at 6,000 km

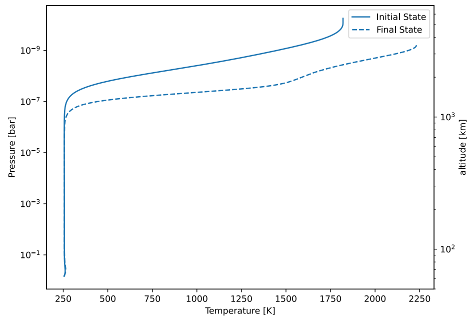

(a) $\log(X_{\mathrm{H_20}}) = -3.70$

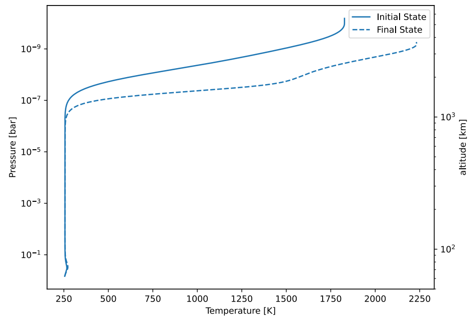

(b) $\log(X_{\mathrm{H_20}}) = -2.70$

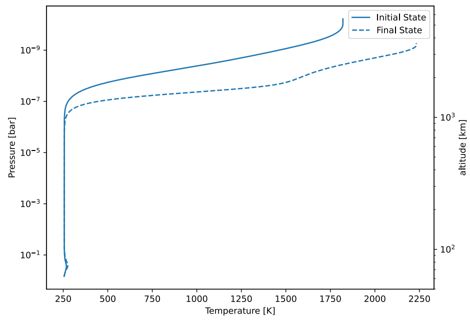

(c) $\log(X_{\mathrm{H_20}}) = -2.30$

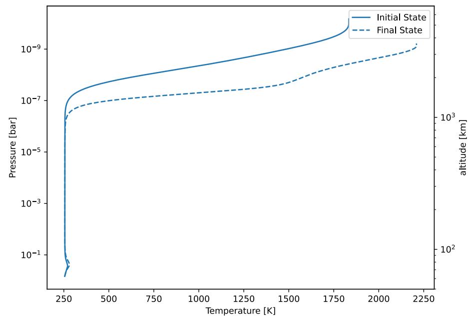

(d) $\log(X_{\mathrm{H_20}}) = -2.00$

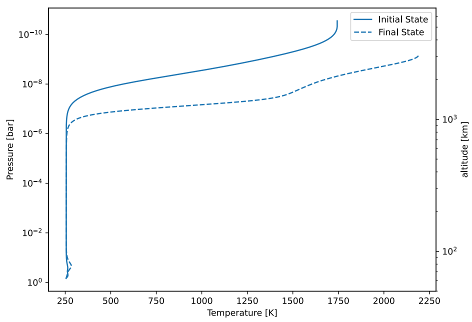

(e) $\log(X_{\mathrm{H_20}}) = -1.70$

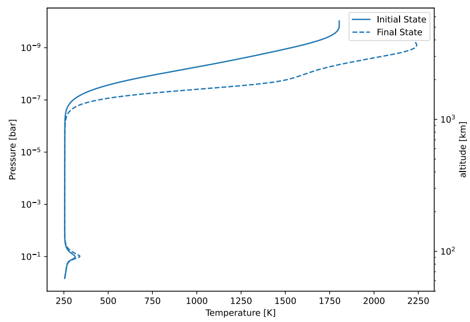

(f) $\log(X_{\mathrm{H_20}}) = -0.82$

Figure A.2: Pressure-temperature profiles for different water abundances, exobase at 7,000 km

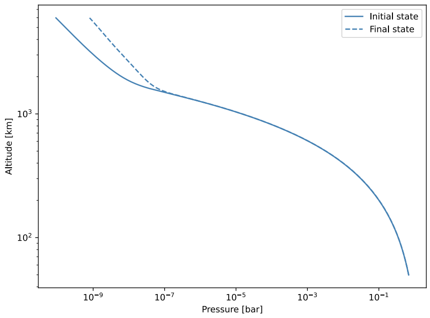

(a) $\log(X_{\mathrm{H_20}}) = -3.70$

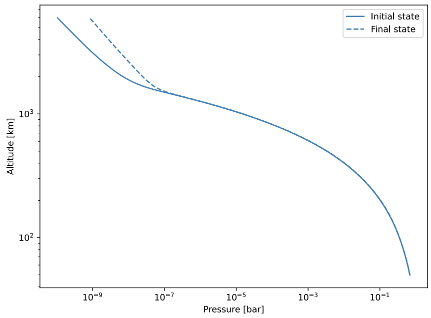

(b) $\log(X_{\mathrm{H_20}}) = -2.70$

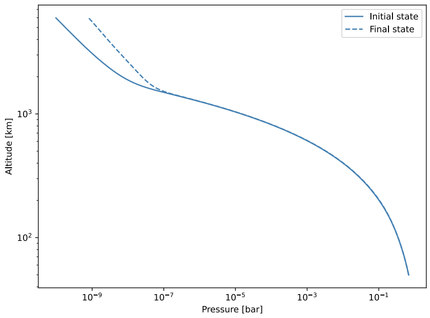

(c) $\log(X_{\mathrm{H_20}}) = -2.30$

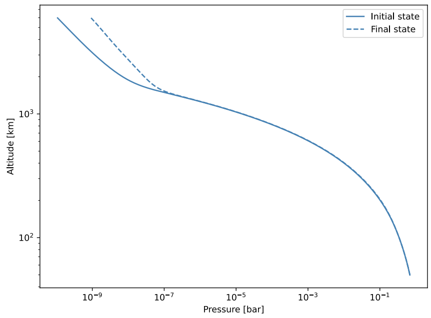

(d) $\log(X_{\mathrm{H_20}}) = -2.00$

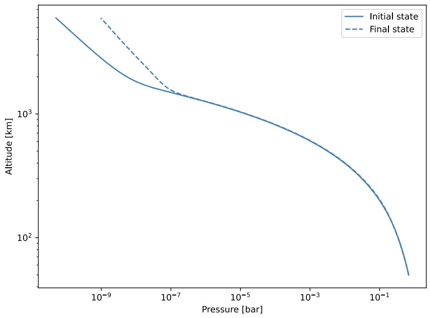

(e) $\log(X_{\mathrm{H_20}}) = -1.70$

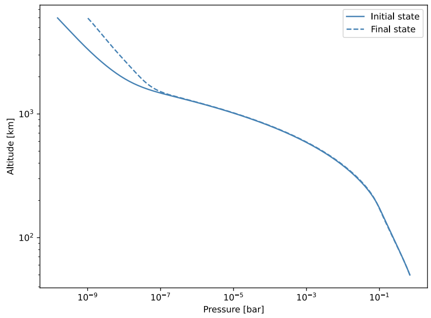

(f) $\log(X_{\mathrm{H_20}}) = -0.82$

Figure A.3: Pressure-altitude profiles for different water abundances, exobase at 6,000 km

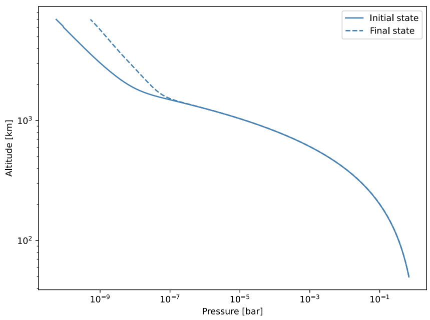

(a) $\log(X_{\mathrm{H_20}}) = -3.70$

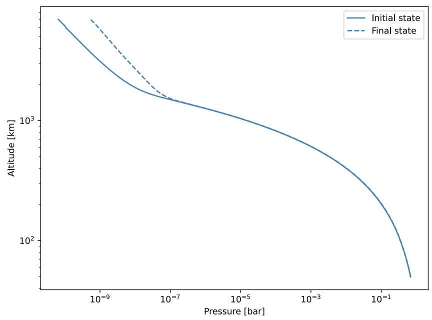

(b) $\log(X_{\mathrm{H_20}}) = -2.70$

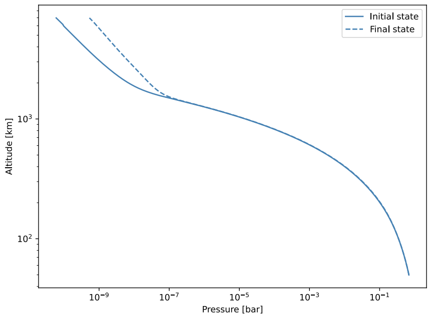

(c) $\log(X_{\mathrm{H_20}}) = -2.30$

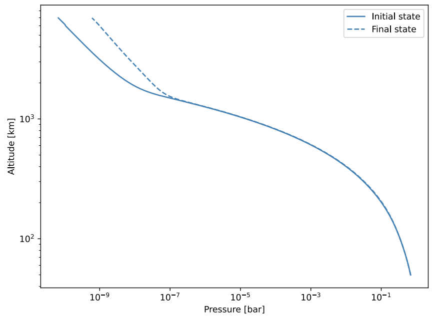

(d) $\log(X_{\mathrm{H_20}}) = -2.00$

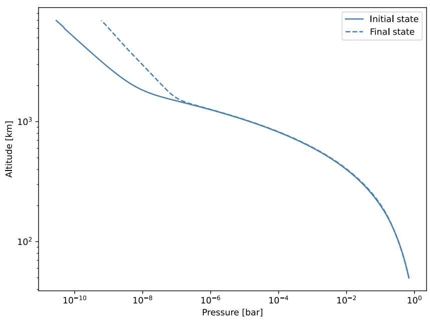

(e) $\log(X_{\mathrm{H_20}}) = -1.70$

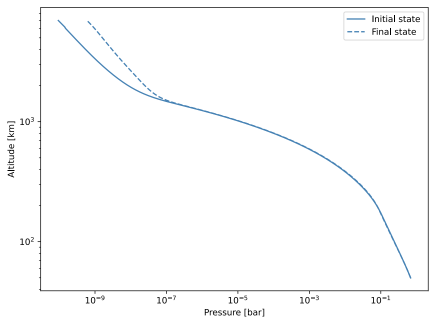

(f) $\log(X_{\mathrm{H_20}}) = -0.82$

Figure A.4: Pressure-altitude profiles for different water abundances, exobase at 7,000 km

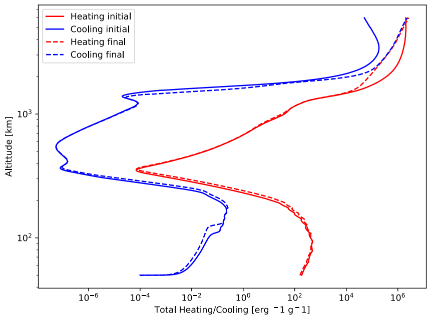

(a) $\log(X_{\mathrm{H_20}}) = -3.70$

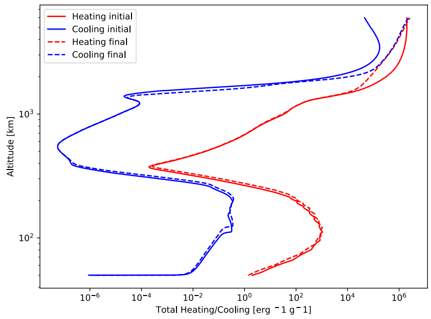

(b) $\log(X_{\mathrm{H_20}}) = -2.70$

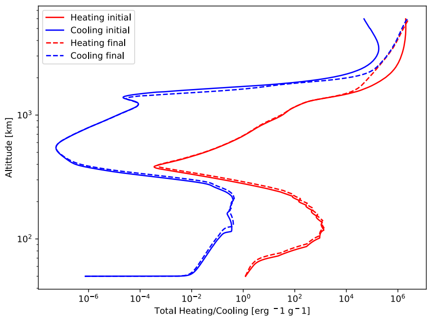

(c) $\log(X_{\mathrm{H_20}}) = -2.30$

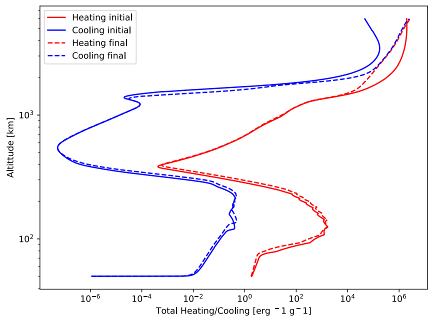

(d) $\log(X_{\mathrm{H_20}}) = -2.00$

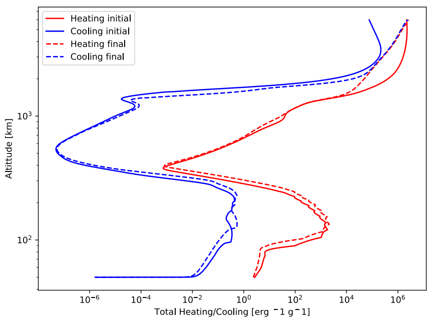

(e) $\log(X_{\mathrm{H_20}}) = -1.70$

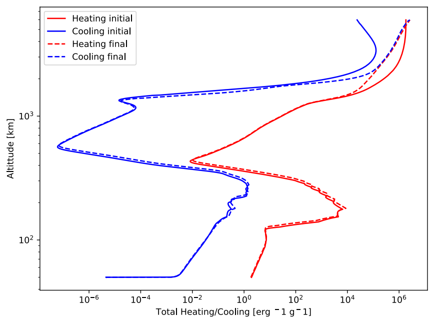

(f) $\log(X_{\mathrm{H_20}}) = -0.82$

Figure A.5: Total heating and cooling for different water abundances, exobase at 6,000 km

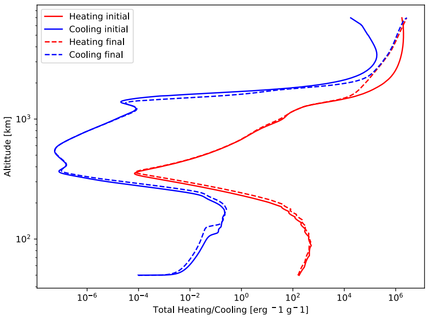

(a) $\log(X_{\mathrm{H_20}}) = -3.70$

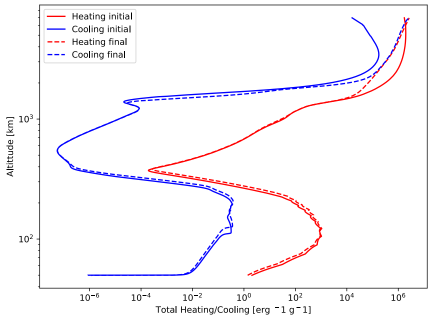

(b) $\log(X_{\mathrm{H_20}}) = -2.70$

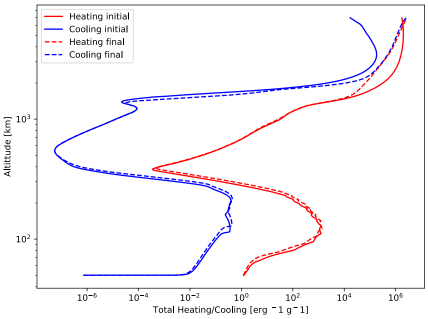

(c) $\log(X_{\mathrm{H_20}}) = -2.30$

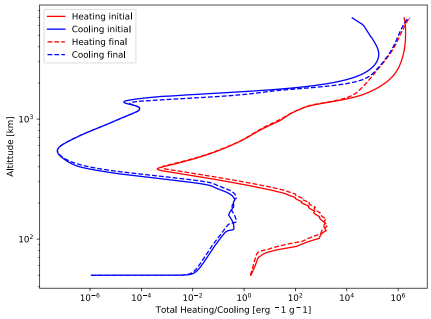

(d) $\log(X_{\mathrm{H_20}}) = -2.00$

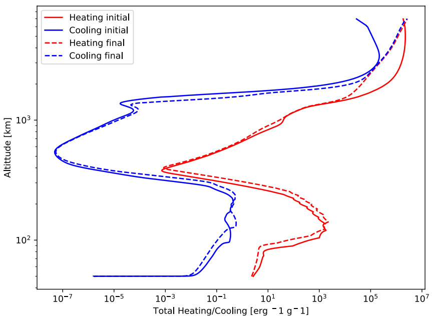

(e) $\log(X_{\mathrm{H_20}}) = -1.70$

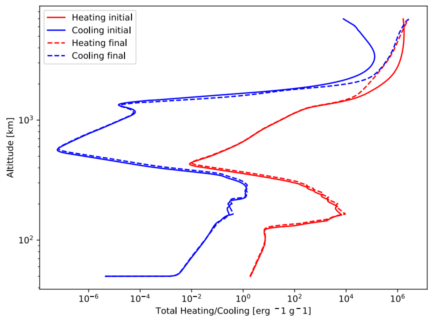

(f) $\log(X_{\mathrm{H_20}}) = -0.82$

Figure A.6: Total heating and cooling for different water abundances, exobase at 7,000 km

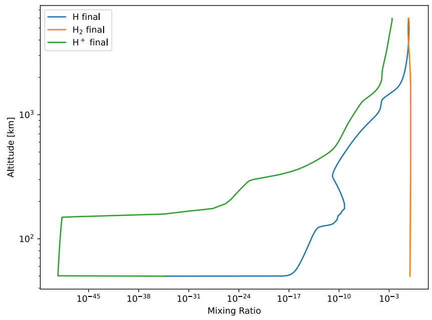

(a) $\log(X_{\mathrm{H_20}}) = -3.70$

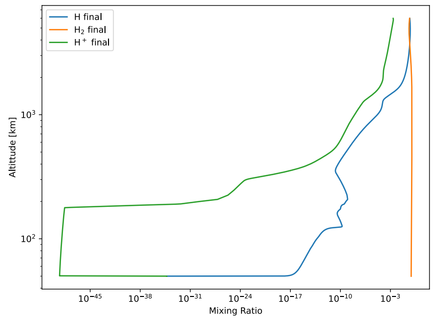

(b) $\log(X_{\mathrm{H_20}}) = -2.70$

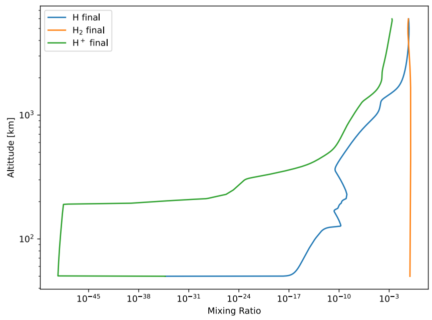

(c) $\log(X_{\mathrm{H_20}}) = -2.30$

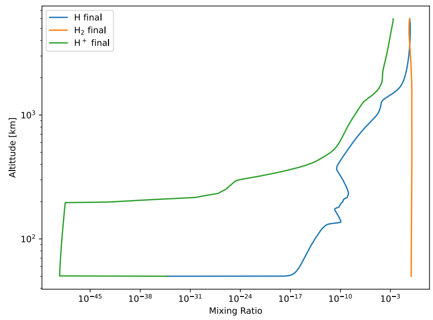

(d) $\log(X_{\mathrm{H_20}}) = -2.00$

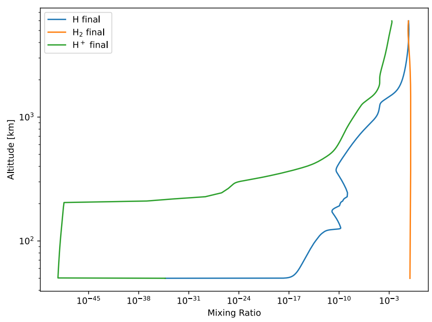

(e) $\log(X_{\mathrm{H_20}}) = -1.70$

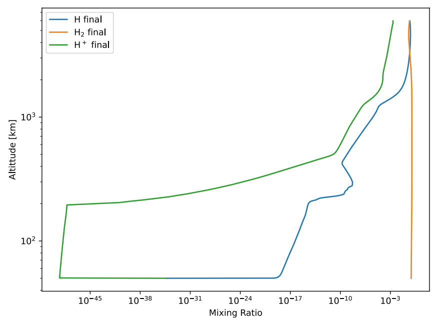

(f) $\log(X_{\mathrm{H_20}}) = -0.82$

Figure A.7: Species profile of the three most abundant species for different water abundances, exobase at 6,000 km

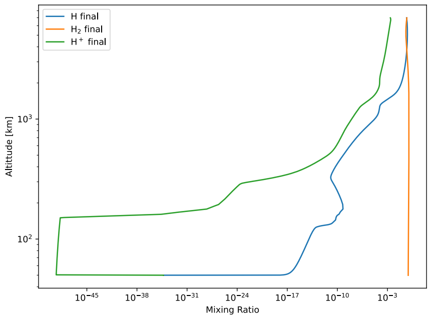

(a) $\log(X_{\mathrm{H_20}}) = -3.70$

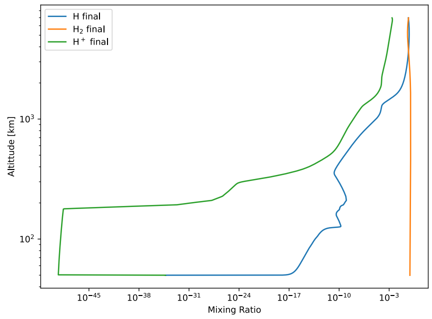

(b) $\log(X_{\mathrm{H_20}}) = -2.70$

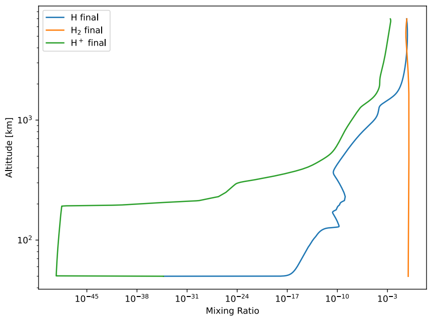

(c) $\log(X_{\mathrm{H_20}}) = -2.30$

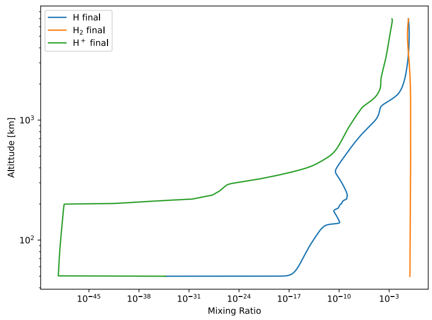

(d) $\log(X_{\mathrm{H_20}}) = -2.00$

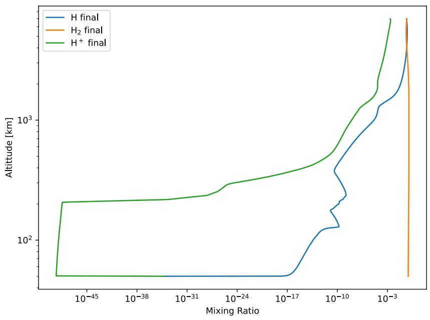

(e) $\log(X_{\mathrm{H_20}}) = -1.70$

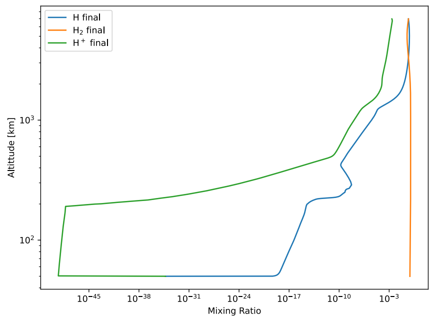

(f) $\log(X_{\mathrm{H_20}}) = -0.82$

Figure A.8: Species profile of the three most abundant species for different water abundances, exobase at 7,000 km